Summer 7-28-2023

Crustal Structures of Diebold Knoll and Adjacent Juan De Fuca Oceanic Crust from Integration of Seismic, Gravity and Magnetic Data

Md Ariful Islam
University of Nebraska-Lincoln, aislam3@huskers.unl.edu

Crustal Structures of Diebold Knoll and Adjacent Juan De Fuca Oceanic Crust from Integration of Seismic, Gravity and Magnetic Data

By

Md Ariful Islam

A THESIS

Presented to the Faculty of

The Graduate College at the University of Nebraska

In Partial Fulfillment of Requirements

For the Degree of Master of Science

Major: Earth and Atmospheric Sciences

Under the Supervision of Professor Irina Filina

Lincoln, Nebraska

August, 2023

Crustal Structures of Diebold Knoll and Adjacent Juan De Fuca Oceanic Crust from Integration of Seismic, Gravity and Magnetic Data

Md Ariful Islam, M.S.

University of Nebraska, 2023

Advisor: Irina Filina

Cascadia Subduction Zone (CSZ) has a long history of devastating earthquakes as the Juan de Fuca plate subducts beneath North America, where an imminent megathrust earthquake is expected. Compared to other subduction zones, CSZ exhibits unusually low seismic activity, particularly in the central region with respect to relatively high seismicity zones to the north and south. Some researchers attribute this behavior to subducted seamounts, although their impact on seismicity remains poorly understood and highly debated in the literature. Examining subducted seamounts is challenging due to complexity of the overburden strata. That is why this study focuses on an isolated not-yet-subducted intraplate seamount known as the Diebold Knoll, located approximately 60 km west of the deformation front. Seismic reflection, gravity, and magnetic data were acquired over that seamount during the cruise RR1718.

The first objective of this research was to determine heterogeneities in physical properties of oceanic crust resulted from addition of the seamount by integrated geophysical analysis along two intersecting profiles. The second objective was to reveal the tectonic history of the Diebold Knoll by combining magnetic polarity reversals with cross-cutting relationship analysis of seismic structures and constrained by the nearby ocean drilling sites.

These models revealed that Diebold Knoll does not require complete isostatic compensation. Instead, a flat Moho or a less than 1 km thick root is sufficient to satisfy gravity data; both of these Moho geometries are observed in the study area. To achieve a better fit with observed gravity and magnetic anomalies, lower density and magnetic susceptibility values within the top portion of the seamount are required, which are attributed to faulting and hydration. This finding is also in agreement with a recent study that analyzed seismic velocity variations within seamounts. Furthermore, the negative magnetic anomaly of the seamount and the cross-cutting relationships between sedimentary layers and the seamount body indicated that Diebold Knoll is a very young feature formed approximately 0.8-1.8 Ma.

Contents

Chapter - 1: Introduction 1

1.1 Study area 1

1.2 Motivation for this study 3

1.3 Objectives 6

Chapter - 2: Geological background 8

2.1 Juan de Fuca plate 8

2.2 Cascadia Subduction Zone (CSZ) 10

2.3 Seamounts on the JdF plate 11

2.4 Magma source for intraplate seamounts 15

2.5 Evidence of seamount subduction in CSZ and its effect on subduction process 16

Chapter - 3: Geophysical Datasets 18

3.1 Seismic Data 18

3.1.1 Multi-channel Seismic (MCS) data 18

3.1.2 Seismic refraction data 22

3.2 Gravity anomaly data 24

3.3 Magnetic anomaly data 26

3.4 Bathymetry data 27

3.5 Ocean drilling data 29

Chapter - 4: Methodology 32

4.1 2.75D Geophysical modeling 32

4.2 Geological constrains 36

4.3 Isostatic modeling 37

Chapter - 5: Results 40

5.1 Tectonic history of Diebold Knoll and age approximation 40

5.2 2.75D integrated models and physical properties 41

5.2.1 Scenario 1: Stable oceanic crust, flat Moho beneath Diebold Knoll with no crustal bending 42

5.2.2 Scenario 2: Crustal bending from Airy isostatic equilibrium calculation ... 46

5.2.3 Scenario 3: Root thickness from analogous regional examples 47

Chapter - 6: Discussion 49

6.1 Isostatic compensation of seamounts on JdF 49

6.2 Age of the Diebold Knoll 51

6.3 Physical properties of the Diebold Knoll: 57

Chapter - 7: Conclusions 59

List of Figures

Figure 1.1. 2

Figure 1.2. 5

Figure 2.1. 8

Figure 2.2. 13

Figure 2.3. 14

Figure 2.4. 17

Figure 3.1. 20

Figure 3.2. 22

Figure 3.3. 23

Figure 3.4. 25

Figure 3.5. 28

Figure 3.6. 30

Figure 4.1. 35

Figure 4.2. 37

Figure 5.1. 41

Figure 5.2. 43

Figure 5.3 44

Figure 5.4. 47

Figure 5.5. 48

Figure 6.1. 52

Figure 6.2. 54

Figure 6.3. 55

List of Tables

Table 1: Seismic velocities for different layers: 21

Table 2: Summery of density and age from DSDP-18-174-A..... 31

Table 3: Physical properties from previous studies. 38

Table 4: Physical properties resulting from integrated models. 45

Chapter - 1: Introduction

1.1 Study area

Subduction zones, where one tectonic plate subducts beneath another, are well-known for large devastating earthquakes and related geological hazards like tsunamis and landslides (Heaton and Hartzell, 1987; Stern, 2002; Burgmann et al., 2005; Perfettini et al., 2010). This study focuses on the Cascadia Subduction Zone (CSZ) where oceanic Juan de Fuca (JdF) plate subducts beneath the continental portion of the North American plate (Figure 1.1). The specific geologic feature for this investigation is the Diebold Knoll (DK), a small volcanic seamount ~60 km west of the deformation front of the CSZ. The Diebold Knoll is situated in the southeastern part of the Juan de Fuca oceanic plate (43.883333° N, -126.166667° W). It is an isolated, intraplate seamount with a relief of approximately 750 m from the surrounding seafloor (as shown in the inset of Figure 1.1) and ~1400 m from the top of the JdF crust. The goal of the study is to investigate the tectonic history of the Diebold Knoll and variations in crustal properties associated with its formation.

The Diebold Knoll is categorized as a "knoll" due to its height of less than 1000 meters and its flat top (Buchs et al., 2016). This seamount complex comprises of four interconnected volcanic peaks, two of which are exposed above sediments (as seen in the inset map in Figure 1.1), one nearly buried, and one completely covered by sedimentary deposits. The whole seamount complex is approximately 15 km long and 8 km wide.

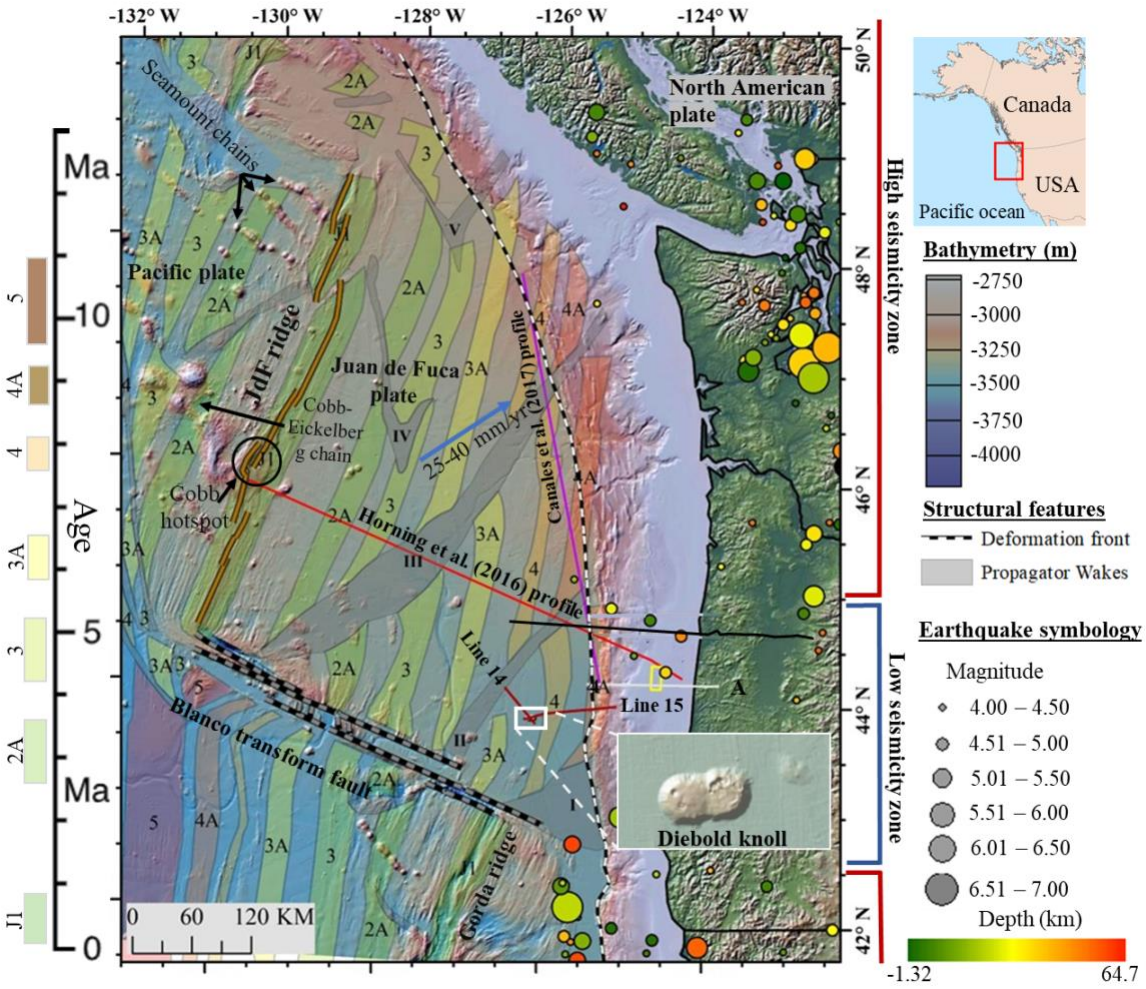

Figure 1.1: Regional map of the CSZ with the eastern boundary marked by the deformation front. Key tectonic elements are shown over shaded bathymetry grid from GeoMapApp based on GMRT 4 (Ryan et al., 2009). Magnetic isochrons are adopted from Wilson (2002). Gray shaded area outlines the propagator wakes (Wilson, 1988; 2002). The thick black line is the location of the refraction profile from Trehu et al. (1994) shown in Figure 3.3b. Profile AA' from Trehu et al. (2012) is shown as the white line with the location of interpreted subducted seamount inside the yellow rectangle. Circles of different colors show locations of earthquakes with magnitude 4.0 and above recorded from 1918 to 2022 from the USGS earthquake catalog (https://earthquake.usgs.gov/), depth of earthquakes is indicated by color and magnitude by size of the circles. The inset map shows a zoomed in view of the Diebold Knoll. Heck, Heckle and Springfield seamounts (from north to south respectively on the northwest corner of the map) and location of Cobb hotspot (and Axial seamount) and Cobb-Eickelberg seamount chain are also indicated.

1.2 Motivation for this study

The Cascadia Subduction Zone is characterized by a large number of earthquakes as shown in Figure 1.1 (Heaton and Hartzell, 1987; Dragert et al., 1994; Miller et al., 2002; Parsons et al., 2005; Schmalzle et al., 2014). However, compared to other subduction zones, the CSZ has much lower seismicity and the seismic events are not equally distributed along this margin (Heaton and Kanamori, 1984; Weaver and Shedlock, 1991; Trehu et al., 1994). There are high seismicity zones on the northern and southern parts of the CSZ (Figure 1.1), whereas the central part is anomalously quiet (Rogers et al., 1991; Porritt et al., 2011; Han et al., 2018; Bodmer et al., 2018). The Juan de Fuca and North American plates are thought to be locked or partially locked along the CSZ (McCaffrey et al., 2007; Burgette et al., 2009; Schmalzle et al., 2014).

There are historical evidences from paleoseismic studies suggesting repeated megathrust earthquakes occurred during the Holocene along the CSZ (Heaton and Hartzell, 1987; Rogers, 1988; Clague, 1997; Kirby et al., 2002; Goldfinger et al., 2003; Ludwin et al., 2005; Melgar, 2021). Significant earthquake events of magnitude ~9 (Atwater, 1987; Goldfinger et al., 2003) occur roughly every 220-550 years (Atwater and Hemphill-Haley, 1997; Goldfinger et al., 2017). The last great megathrust earthquake happened on January 26th, 1700 A.D., with about 9 M_w (Nelson et al., 1995; Atwater and Hemphill-Haley, 1997), which was also recorded as tsunami waves in Japan that propagated across the Pacific Ocean (Satake, 2003; Atwater et al., 2015).

In addition, many studies suggest that a great megathrust earthquake of similar magnitude is expected in the near future in this margin (e.g., Rogers, 1988; Adams, 1990; Adams and Weichert, 1994; Hyndman et al., 1996; Mazzotti, 2004), which poses a significant risk to the densely populated coastal regions along the western coast of North America. This study aims to provide a better understanding of an important geologic feature on the subducting oceanic slab (the Diebold Knoll) that may serve as analog to the ones that are already in the subduction domain and influence seismicity pattern.

Seamounts and bathymetric highs are scattered on the subducting JdF plate (Figure 1.1). There are no seamount chains on the JdF plate (Figure 2.2) in contrast to the Pacific plate on the other side of the JdF ridge. The presence of isolated seamounts introduces complexities to subduction dynamics (Figure 1.2). According to some studies, seamounts may increase the likelihood of larger earthquakes by accumulating stress, causing plate locking, contributing to subduction zone segmentation, and eroding the crust of the overriding plate (Scholz et al., 1997; Kodaira et al., 2000; Cummins et al., 2002; Abercrombie et al., 2003; Bilek et al., 2003; Robinson et al., 2006; Mochizuki et al., 2008; Singh et al., 2011). In contrast, other studies suggest that the subduction of seamounts can distribute stress over a wide region around the subducting feature by creating a fracture network in the overlying plate (Figure 1.2), which may lead to aseismic slip behavior (Wang and Bilek, 2011, 2014). The effect of a subducting seamount may also vary depending on the presence or absence of the crustal root as it influences the seamount's buoyancy. Therefore, it is crucial to comprehend the crustal

architecture, physical properties, and tectonic evolution of seamounts no matter how they impact the subduction process and earthquake distribution. This understanding, in turn, can shed light on how variations in physical properties of oceanic crusts complicated by the presence of seamounts, as well as the age of these features, might influence the subduction process.

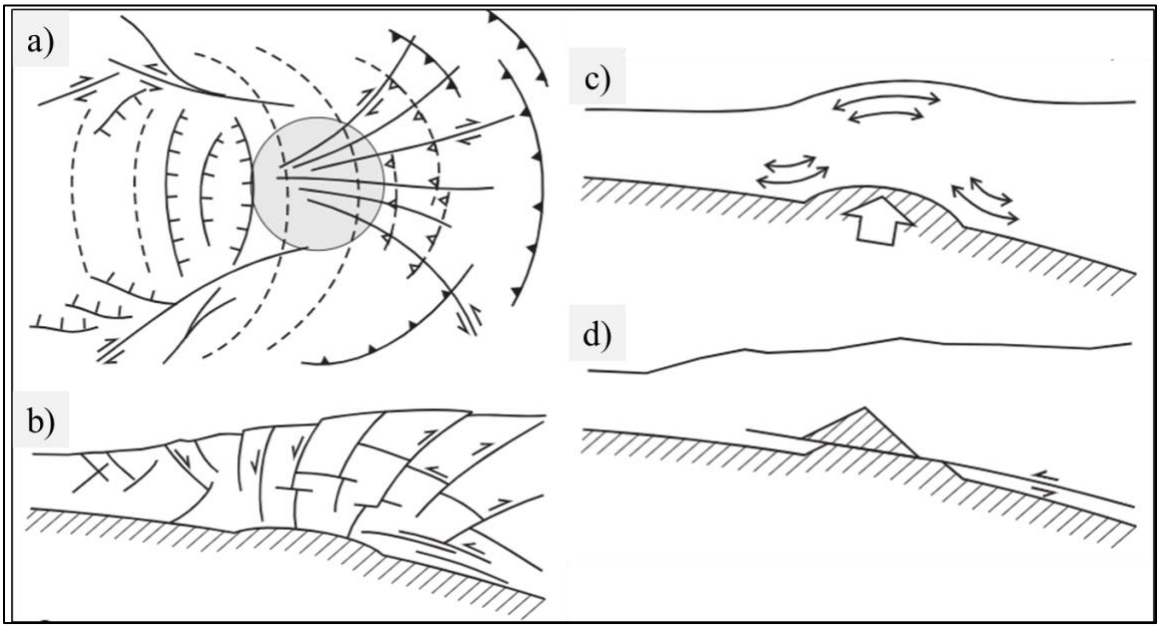

Figure 1.2: Possible scenarios of the seamount behavior during subduction adopted from Wang and Bilek (2011). The first scenario suggests the development of a fracture network on the upper plate with panel a) showing the map view (based on Dominguez et al., 1998) and panel b) the representative cross-section. The scenario in panel c) illustrates flexure of an elastic upper plate, while d) shows decapitation of the seamount. The last two scenarios are considered incorrect and unlikely respectively by Wang and Bilek (2011).

It is challenging to image the seamounts that are within deformation zones because these are buried by thick, folded, and faulted sedimentary deposits. In contrast, the Diebold

Knoll offers an opportunity to study a seamount that has not yet been subducted but is on its way toward the Cascadia Subduction Zone. Therefore, this seamount could provide important insights into heterogeneities within subducting oceanic crust that impact the overall subduction process.

1.3 Objectives

The Diebold Knoll developed in an intraplate setting, and its magma source, age, and overall formation are poorly understood. This study aims to integrate various geophysical methods to achieve two main objectives.

The first objective is to determine how the formation of the seamount altered the hosting oceanic crust. In particular, this objective addresses the variations in physical properties of the crust and seamount complex, such as bulk density and magnetic susceptibility. In addition, crustal heterogeneities caused by the formation of seamount complex can affect the strength of the subducting slab, which, in turn, impacts the behavior of the downgoing plate. Changes in crustal architecture associated with the formation of the seamount are also investigated (namely the presence or absence of a crustal root). To achieve this objective, integrated geophysical modeling for two profiles crossing over the Diebold Knoll was utilized.

T**he second objective** is to investigate the tectonic history and origin of the Diebold Knoll and estimate possible geologic time(s) of its formation. This is important because an older seamount will behave differently than a younger seamount during subduction because they have different crustal strength and root structure. Without scientific drilling

or dredging data over the Diebold Knoll, it is not possible to determine the exact age and tectonic origin of this feature. With no direct constraints, the integration of different geophysical data is the only way to solve this puzzle. Magnetic reversals, combined with limited seismic reflection and nearby drilling data, allowed to derive the most likely geologic scenario for the formation of the Diebold Knoll.

Chapter - 2: Geological background

2.1 Juan de Fuca plate

Prior to the Mesozoic era, the Pacific Plate was surrounded by the Izanagi Plate to the north, the Farallon Plate to the east, the Phoenix Plate to the south, and the American Plate to the west (Atwater, 1989). The Pacific Plate gradually increased in size as these surrounding plates moved towards the north, east, and south, and the Farallon plate became smaller and smaller (Atwater, 1989; Figure 2.1).

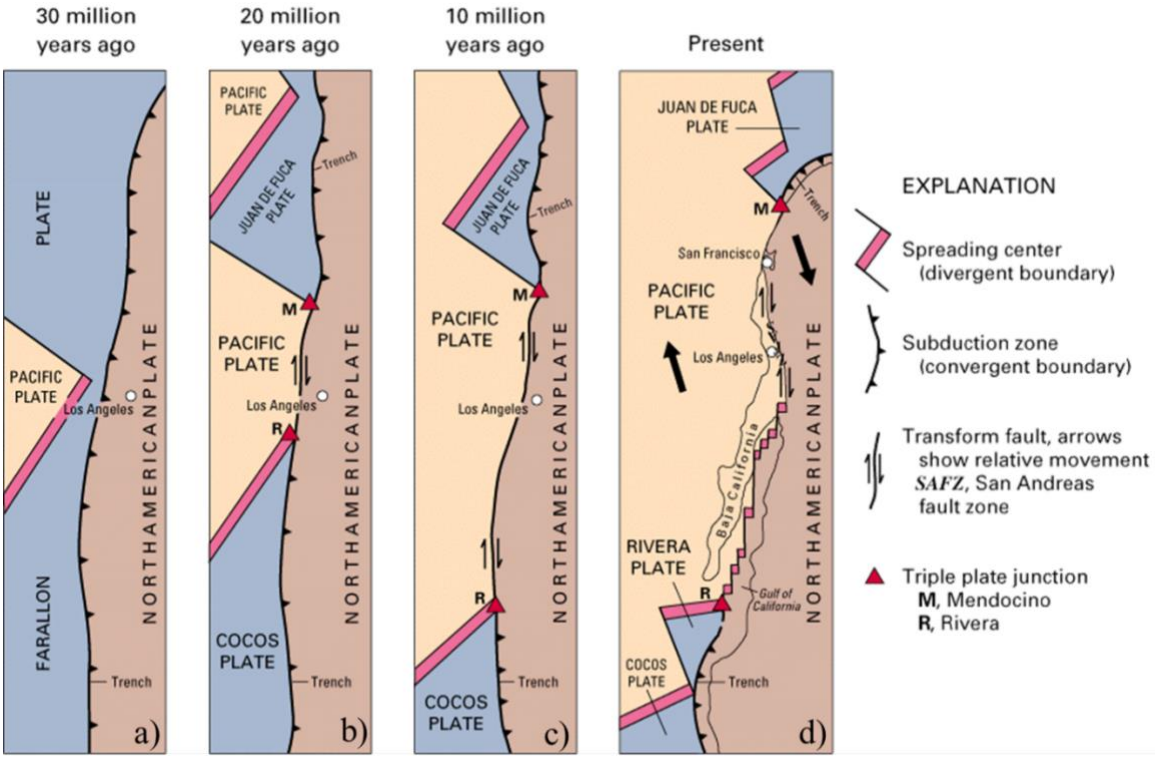

Figure 2.1: Evolution of the Juan de Fuca plate from the Farallon plate through geologic time. The illustration is from https://pubs.usgs.gov/gip/dynamic/Farallon.html based on Irwin and Wallace (1990). The JdF came into existence as the Pacific-Farallon ridge started subducting.

As a result, the Farallon plate became very narrow, and during the Eocene it began to break apart, leading to the formation of the Vancouver Plate to the north and the Nazca Plate to the south (Atwater, 1989). This also triggered fragmentation of the Pacific-Farallon Ridge as it approached the subduction zone (Atwater, 1989) as shown in Figure 2.1a. As the Farallon Plate continued to subduct, the Farallon-Pacific ridge came into contact with the subduction zone, giving rise to the Cocos plate, the Juan de Fuca Plate, and the Explorer Plate (Figure 2.1). The Juan de Fuca plate system includes the Explorer, the Juan de Fuca and the Gorda plates (DiPietro, 2018).

Plate tectonic reconstructions indicate that the Farallon plate disintegrated and gave rise to the JdF plate during the Oligocene period, approximately ~30 million years ago (Wilson, 1988; Atwater, 1989; Govers and Meijer, 2001). The current Juan de Fuca plate is relatively young, with a maximum age of 9 million years at the southeastern part (Rogers, 1988; Wilson, 1988, 2002). The JdF plate is currently moving northeastward (~N49°E) towards the North American plate (McCrory, 2000; DiPietro, 2018) and subducting at a rate of about 40 mm/year at the northern part of the plate and as low as 25 mm/year at the southern end of the Cascadia Subduction Zone (DeMets et al., 1990; Govers and Meijer, 2001; Kreemer et al., 2014; Han et al., 2018).

Shih and Molnar (1975) identified a series of ridge jumps between 42°N and 48°N, known as rift propagation. Wilson (1988) referred to these characteristics as propagator wakes (PW) based on the distortions in magnetic anomalies, while Hey (1977) initially established the term "pseudofault" for these features. Figure 1.1 illustrates these

propagator wakes numbered I through IV. Besides these PWs, numerous pseudofault lineaments (features of similar origin, but with smaller extent) have been observed on the JdF crust (Ashraf, 2021). Nedimović et al. (2009) observed that some JdF plate earthquakes are concentrated near one of the propagator wakes. Additionally, seismic transects have revealed observable faulting within the propagator wakes, suggesting that these zones represent areas of weak oceanic crust (Nedimović et al., 2009). This idea that propagator wakes are zones of weakness is important as they may have provided pathways for magma upwelling for formation of the intraplate seamounts.

2.2 Cascadia Subduction Zone (CSZ)

The Cascadia Subduction Zone stretches from offshore Northern California to offshore Vancouver Island. Although the Cascadia Subduction Zone has been relatively quiet since the advent of seismic recording in terms of megathrust earthquake activity compared to other subduction zones (Rogers et al., 1991; Trehu et al., 2015), it is still capable of producing large earthquakes. Turbidites and other paleoseismic studies by Goldfinger et al. (2003) suggest at least 13 events that ruptured the entire Cascadia margin in the last ~10,000 years. The last occurrence of ~9 M_w earthquake was about 300 years ago (Nelson et al., 1995; Atwater and Hemphill-Haley, 1997; Ludwin et al., 2005) which has become part of Native American legend (Satake et al., 1996). The tsunami created by this earthquake was recorded in Japanese history, which helped determining the size of this earthquake (Satake et al., 1996; Atwater et al., 2015).

The CSZ can be divided by two east-to-west boundaries along latitudes of 43°N and 46°N (Porritt et al., 2011; Schmalzle et al., 2014) into the northern (Washington and southern British Columbia), central (Oregon), and southern (Northern California) segments. The northern and southern segments have generated much more earthquakes than the central quiet zone (Figure 1.1). GPS (Global Positioning System) investigation of plate movement show that central Cascadia represents a weakly locked seismogenic zone with consistent partial creeping (Audet et al., 2010), but it is still unclear what is causing the decrease in plate locking between the JdF and North American plate. Some hypotheses include changes in frictional shear strength along the strike (Perfettini and Ampuero, 2008; Perfettini et al., 2010), geometrical features (seamounts and bathymetric highs; shown in FiguresFigure 1.1 &Figure 2.2) on the subducting slab (Trehu et al., 1994; Song and Simons, 2003), and long-term slip history at the plate interface (Burgmann et al., 2005).

2.3 Seamounts on the JdF plate

There are several seamounts in the study area (as seen in Figure 1.1) with the majority of them clustered around the JdF spreading center. The JdF Ridge is approximately 1000 km long and is characterized by a series of rift valleys, volcanic cones, and seamount chains. Seamounts around the JdF ridge can be divided into two types: seamount chains and isolated seamounts. All seamount chains, such as the Cobb–Eickelberg, Heck, Heckle and Springfield seamounts (Figure 1.1Figure 2.2) originate at the JdF ridge and reside on

the Pacific plate to the west of the ridge. The Cobb-Eickelberg Seamount Chain is the most prominent seamount chain in the region that extends for over 1800 km to the west of the Juan de Fuca Ridge (Chadwick, 2005). It is thought to have been initiated ~33 million years ago (Chadwick, 2005) and consists of more than a dozen individual seamounts. The seamounts in the Cobb-Eickelberg Chain have been studied extensively, and their geological characteristics have been well documented. The Axial Seamount is a submarine volcano collocated with the Juan de Fuca Ridge and the Cobb hotspot (West et al., 2003). It is the most active volcano on the ridge and has erupted at least 9 times in the last 40 years (Wilcock et al., 2016).

On the JdF plate, there are no seamount chains observed on the seafloor. Instead, there are several isolated intraplate seamounts (buried and exposed) on the JdF plate. These seamounts head toward the CSZ, and there is evidence of those seamounts subducting along with plate (Tréhu et al., 2012; Lee et al., 2022). Many seamounts have been discovered by geophysical surveys such as the Cascadia Seismic Imaging Experiment - CASIE 21 seismic survey (Carbotte et al., 2022) and MGL1211 (Horning et al., 2016) as shown in Figure 2.2. These surveys were able to image the Moho beneath some of these seamounts. Most of these seamounts are buried under sedimentary deposits. Lee et al. (2022) reported presence of several seamounts along the CSZ from analysis of CASIE 21 seismic reflection data. Except for the seamount PD11/MCS03, all other seamounts from Lee et al. (2022) show no sign of crustal flexure (i.e., root) beneath them.

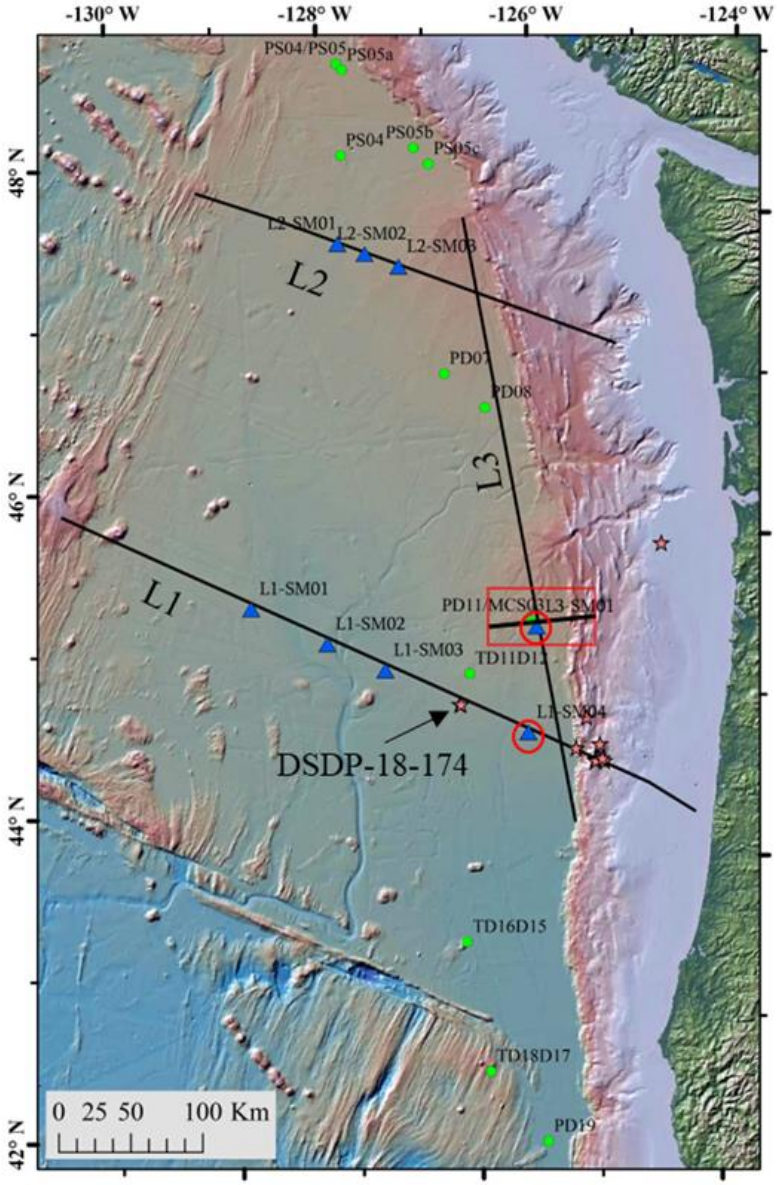

Figure 2.2: Seamounts imaged during two seismic surveys (MGL1211 and CASIE21). The ones derived from CASIE21 (Carbotte et al., 2022; Lee et al., 2022) are shown in green circles; the blue triangles indicate the location of seamounts/bathymetric highs imaged during cruise MGL1211 (Han et al., 2016; Horning et al., 2016; Canales et al., 2017). Seamounts are given labels based on which profile they are found, and seamounts with apparent root are shown in red circles. The black line inside red box marks the location of profile PD11 and seamount PD11/MCS03 (this may also coincide with seamount L3-SM1 from MGL1211) which is shown in Figure 2.3 DSDP (Deep Sea Drilling Project) and ODP (Ocean Drilling Project) sites are indicated by the orange stars.

This seamount (PD11/MCS03) rises ~1.14 km above the crust (Figure 2.33) and the estimated root is up to 1 km thick. Except for seamount PD11/MCS03, all other seamounts from Lee et al. (2022) show no sign of crustal flexure (i.e., root) beneath the seamount. Seamount L1-SM04 has a height of ~320 m above the basement and ~230 m thick root, estimated from interpreted seismic profiles from Han et al. (2016). For both seamounts, the root-to-height ratio comes up as 0.65. Since the Diebold Knoll is situated on similar tectonic setting as PD11/MCS03 seamount from Lee et al. (2022), this ratio was used to estimate potential thickness of the root beneath it for one of potential geological scenarios of this study.

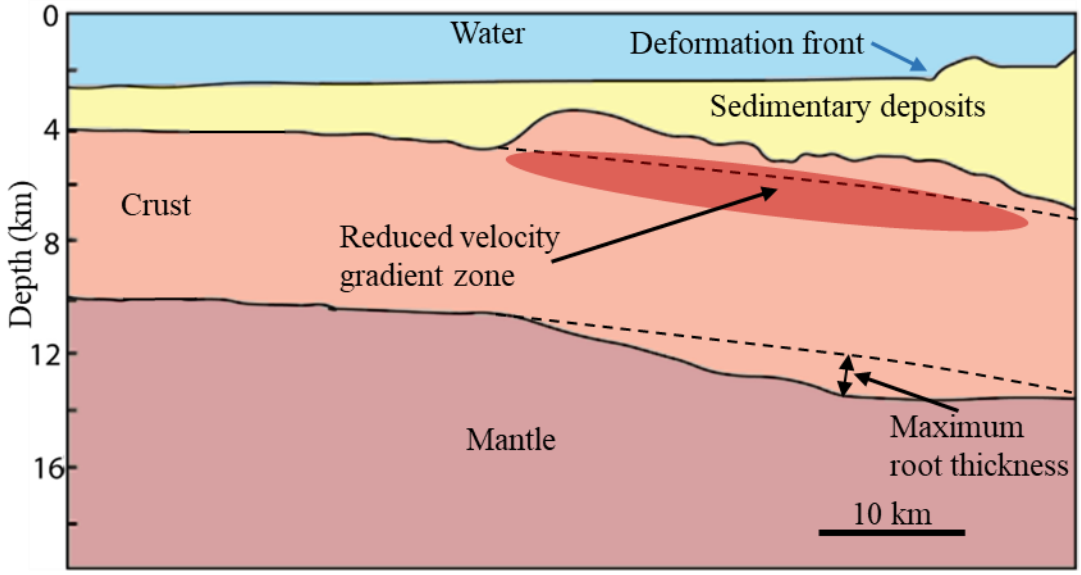

Figure 2.3: A schematic diagram for seismic profile PD11 presented by Lee et al. (2022) showing buried seamount PD11/MCS03 (see location in Figure 2.2). Notably, the seamount is covered by the abyssal plain sediments and has a pronounced crustal root. Oval shape indicates reduced velocity gradient zone within the seamount complex.

2.4 Magma source for intraplate seamounts

Intraplate seamounts are common features on the ocean floor. While their formation is not related to spreading centers, they are often interpreted to originate from rising mantle plumes or hotspots (Schmidt et al., 2000). However, there are intraplate seamounts that are not related to hotspots either. The Diebold knoll cannot be associated with any known hotspots, so it represents a non-hotspot intraplate volcano. Research on these non-hotspot intra-plate seamounts is relatively limited, and the understanding of their formation processes is still evolving. Some studies suggest that these seamounts may result from localized lithospheric weaknesses due to lithospheric stretching and boudinage (Sandwell and Dunbar, 1988; Sandwell et al., 1995), thermal contraction of the plate (Gans et al., 2003; Sandwell and Fialko, 2004), thermo-elastic cracking and melting anomalies in the asthenosphere (Forsyth et al., 2006) which cause mantle upwellings not necessarily associated with deep mantle plumes or hotspots.

Kipf et al. (2014) described another mechanism for the formation of intraplate seamounts by continental insulation flow that helps bringing magma material underneath the oceanic crust, and crustal weak zones facilitating effusive eruptions. However, this scenario is unlikely for the magma source of the Diebold Knoll, as it assumes continental material from a passive margin getting into shallow oceanic mantle. Although, zones of crustal weakness are documented on the Juan de Fuca plate (Ashraf, 2021). In particular, evidence of crustal scale faults has been interpreted from seismic imaging within propagator wakes (Nedimović et al., 2009). Numerous pseudofaults have been identified

on the Juan de Fuca plate from potential field analysis by Ashraf (2021). These faults may serve as pathways for magma upwelling. However, the source of magma remains poorly understood.

2.5 Evidence of seamount subduction in CSZ and its effect on subduction process

The effects of seamounts on subduction process remains highly debated in the literature. Figure 1.2 summarizes four hypothetical scenarios of seamount behavior when they enter the subduction zone. Wang and Bilek (2011) argued against the commonly held idea that subducted seamounts cause large earthquakes because they have to overcome extreme resistance during subduction (Cloos et al., 1992; Scholz and Small, 1997). Some studies described in Wang and Bilek (2011) found that actively subducting seamounts can create stress concentrations that promote and occasionally generate large earthquakes. However, they also found that the majority of already subducted seamounts can act as barriers that prevent the propagation of earthquake ruptures. This is also consistent with other similar studies of the southern Japan Trench, the Mariana Trench, the Hikurangi, Middle America and Java subduction zones (Kodaira et al., 2000; Das and Watts, 2009). Subducting seamounts (and other basement relief features) are also associated with producing numerous earthquakes with magnitude below 7 (Kelleher and McCann, 1976; Fryer and Smoot, 1985; Bell et al., 2010). Wang and Bilek (2011) suggest that subducting seamounts develop a fracture network along their path of subduction (Figure 1.2a), and

by this process it creates favorable conditions for smaller earthquakes and aseismic creep, and unfavorable conditions for large earthquakes, such as megathrust events.

Based on their study of a subducted seamount in the Cascadia Subduction Zone, Tréhu et al., (2012) found concentrations of earthquakes in front (i.e., landward) of subducted seamounts (Figure 2.4), but none of these earthquakes have magnitude greater than 5.

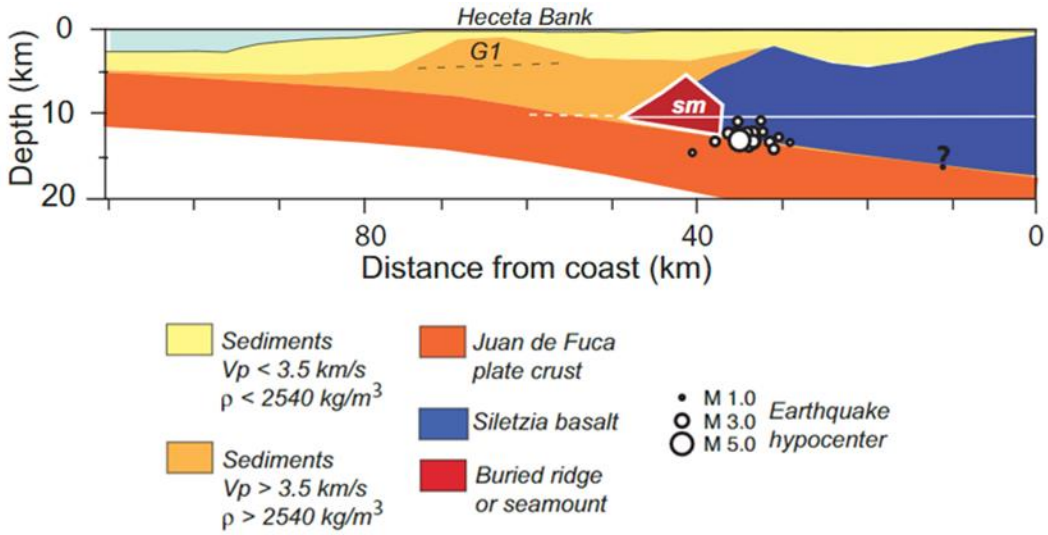

Figure 2.4: Interpreted seamount from seismic p-wave velocity from Tréhu et al. (2012)showing proximity with earthquake clusterClick or tap here to enter text.. Location of the seamount and the profile is indicated in Figure 1.1.

The entire Cascadia region is due for a megathrust earthquake according to some studies (Heaton and Hartzell, 1987; Clague, 1997; Goldfinger et al., 2012; Menichelli et al., 2023). Despite the contradiction in the literature, subducted seamounts have an impact on the overall stress distribution and thus influence the seismicity in the area (Wang and Bilek, 2011). No matter what the effect of such seamounts is, assisting or preventing great earthquakes, Wang and Bilek (2011) conclude that the presence of subducting seamounts should be considered when assessing earthquake hazards in subduction zones.

Chapter - 3: Geophysical Datasets

In this integrated study, a combination of geophysical datasets was utilized, each serving different purposes. The primary datasets used were gravity and magnetic anomalies, and seismic reflection data, which played a crucial role in constructing integrated geophysical models. Furthermore, results from published seismic refraction surveys and the ocean drilling data in the study area were integrated into the analysis. The following sections delve into the specifics of these datasets and the processing methods applied for a thorough understanding of the study area.

3.1 Seismic Data

Both seismic reflection and refraction data were used in this study. Seismic reflection profiles were used directly to provide depth to subsurface layers up to the top of the crust, whereas results from previous seismic refraction studies were used to constrain the depth to Moho and convert reflection data from travel-time to depth.

3.1.1 Multi-channel Seismic (MCS) data

In this project, two 2D seismic profiles from cruise RR1718 (Tominaga et al., 2018),particularly lines 14 and 15, were used. Both profiles cross over the Diebold Knoll (Figure 1.1). Line 14 images the knoll in a NW-SE direction, and line 15 crosses in an E-W direction.

3.1.1.1 MCS data processing from RR1718 cruise

The MCS data collected onboard the *R/V Langseth* were reprocessed to enhance migration and improve image quality. Scripps Multichannel seismic system consisting of a 48-channel GeoEel streamer with a hydrophone spacing of 12.5 m and a shoot spacing of 25 m was employed during the cruise. The total length of the streamer was 600 m. The data was recorded with a sampling rate of 0.5 s for a duration of 8.0 s.

The SEGD data from the shipboard recorder was converted to SEGY format, which was gathered for this study from the Marine Geoscience Data System archive (https://www.marine-geo.org/tools/entry/RR1718). SeismicUNIX software (Cohen and Stockwell, 2021) was utilized for the processing steps that are listed in appendix A. The data was converted into a depth image by OpendTect software (https://www.dgbes.com/software/opendtect) using a simple interval velocity model as described in Table 1.

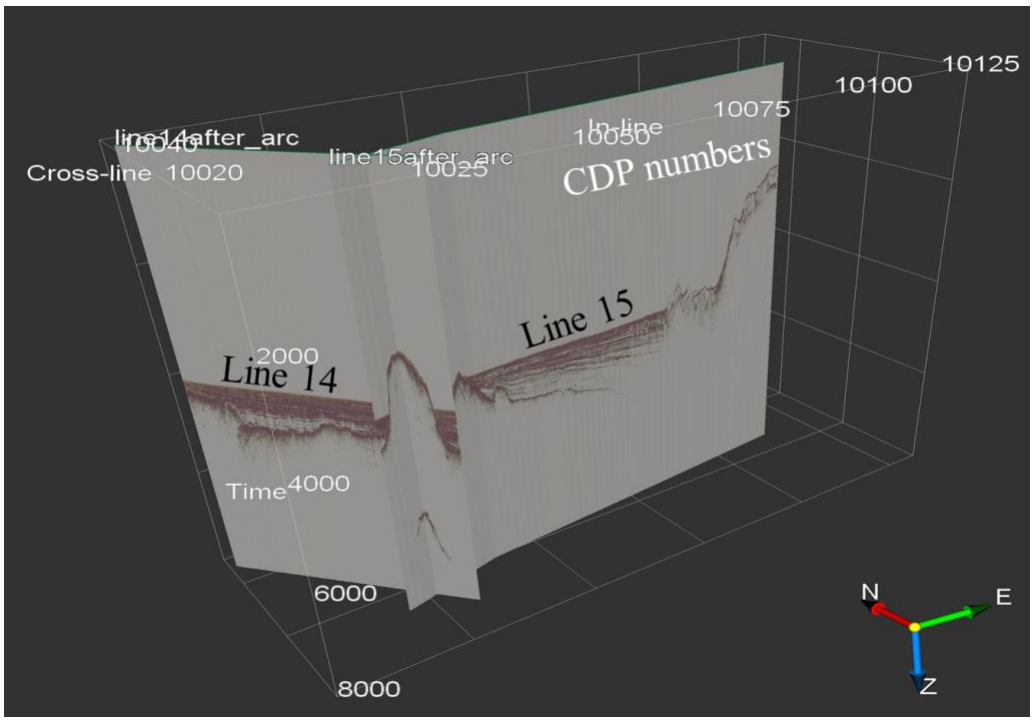

Figure 3.1: Reprocessed seismic lines 14 & 15 from RR1718 survey as viewed in OpendTect (location in Figure 1.1). Basement can be seen bending toward the subduction zone on line 15 and Moho is not imaged on either line.

3.1.1.2 Time to Depth conversion

The seismic image in Two-Way-Travel time (TWT) was divided into three sections based on major layer boundaries, namely the water-seafloor and sediment-crust interfaces. Constant acoustic velocity was assumed for the water layer (Table 1). An increasing velocity gradient was applied from top to bottom for layers two and three to perform time-to-depth conversion, as specified in Table 1. The resulting depth image was utilized for 2.75D modeling in GM-SYS module of OasisMontaj software package, which will be discussed in more detail later.

Table 1: Seismic velocities for different layers:

Layer	**Top velocity (m/s)**	**Bottom velocity (m/s)**	**Sources**
Water	1470		(Telford et al., 1990)
Sediments	1550	2300	(Deep Sea Drilling Project, 1989; Trehu et al., 1994; Horning et al., 2016; Han et al., 2016)
Accretionary prism	1550	5500	
Crust	5500	7000	

3.1.1.3 Reflection profiles from previous studies

Lines 14 and 15 do not show any reflections from the Moho. However, there are several previous studies in the area that imaged Moho (Figure 1.1). One seismic profile from Han et al. (2016) crossing the Juan de Fuca plate from the JdF ridge to the CSZ (Figure 3.2) was used in this study. This profile was part of a joint MCS and OBS (Ocean Bottom Seismometers) data acquisition in 2012 by *R/V Marcus G. Langseth* (cruise MGL1211). This and other wide-angle reflection and OBS studies used much stronger seismic sources and longer hydrophone arrays than the cruise RR1718. As a result, some of these studies imaged reflections from the Moho as shown in Figure 3.2.

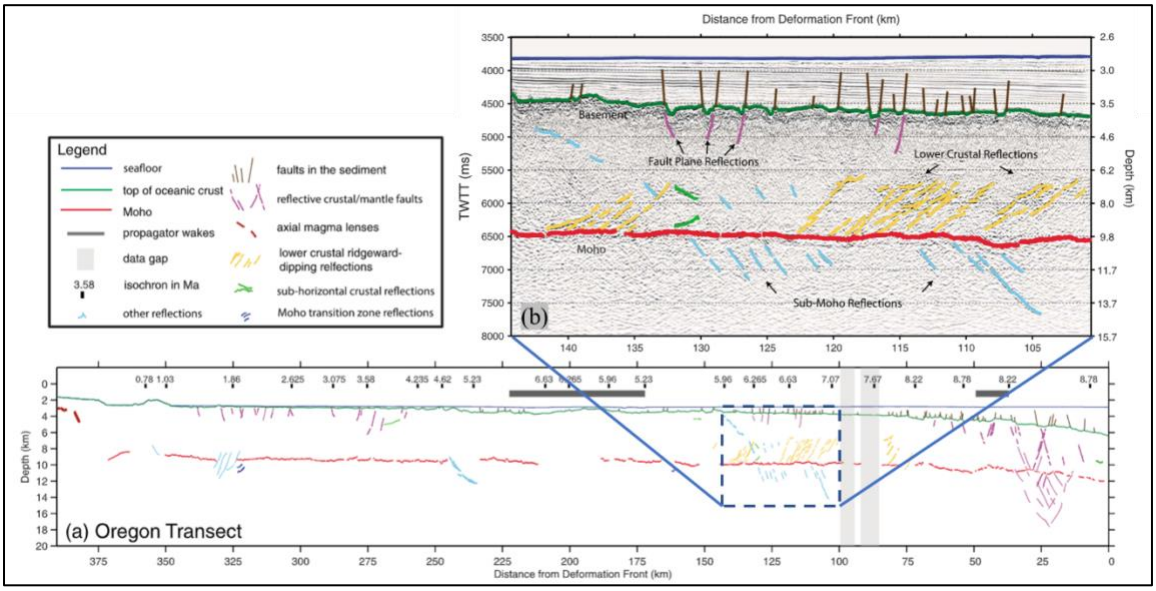

Figure 3.2: (a) Depth converted Oregon transect from Han et al. (2016) showing Moho (in red lines) picked from the two-way travel time MCS profile. (b) A zoomed in portion of the Oregon transect with crustal faults and sub-Moho reflections. Location of this profile is provided in Figure 1.1 and in Figure 2.2 as profile L1.

3.1.2 Seismic refraction data

Cruise OC1206A onboard *R/V Oceanus* was the complementary study to MGL1211 that deployed OBS instruments, and the results were published in Horning et al. (2016). Results from this study were used for time-depth conversion of line 14 and 15. Most other published research (Trehu et al., 1994; Fleming and Trehu, 1999; Gerdom et al.,

2000) has very negligible differences in the thicknesses and seismic velocity structures for the undeformed oceanic crust (Figure 3.3).

Velocity structure: The oceanic layer 1 or pelagic and turbidite sediments has a velocity of 1.7 km/s at the seafloor ((Kulm et al., 1973). The oceanic layer 2 has average crustal velocity of 5.6 km/s (Trehu et al., 1994, 2012; Fleming and Trehu, 1999; Gerdom et al., 2000; Parsons et al., 2005; Horning et al., 2016). Crustal velocity ranges from 7.1km/s to 7.3 km/s within oceanic layer 3 and 7.9-8.1 km/s for mantle below crust.

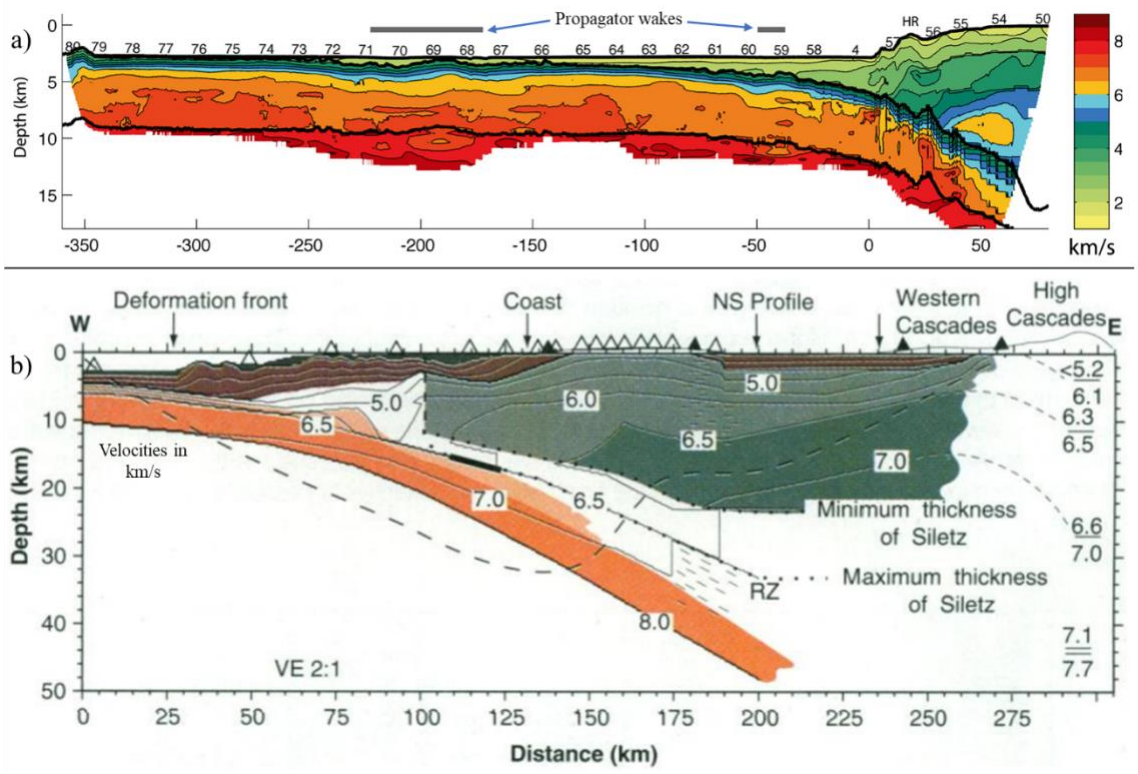

Figure 3.3: Seismic refraction studies on the JdF plate – a) Ridge to trench experiment (Horning et al., 2016) and b) Crustal structure study of the Cascadia forearc from Trehu et al., (1994). Most refraction-derived crustal structures show similar velocities of the JdF crust.

Thickness of crustal layers: Sediment thickness is negligible beyond 250 km west of the deformation front. However, it increases to ~3.1-3.2 km near the trench (Horning et. al., 2016). Average crustal thickness is 6.3 +/- 0.3 km which decreases toward the subduction zone to 6.1+/-0.5 km (Fleming and Trehu, 1999; Gerdom et al., 2000; Horning et al., 2016).

3.2 Gravity anomaly data

In this study, two sets of gravity data were utilized. The first is marine gravity data recorded by the marine BGM-3 gravimeter on *R/V Roger Revelle* during the cruise RR1718 (Tominaga, 2017a; Figure 3.44). Gravity ties for these data were conducted before and after the cruise, with the gravity base station located at Hartfield Marine Center, Newport, Oregon. The gravity value at this base station is 980595.99 mGal.

The second set of gravity data used for this study is global satellite gravity data from Sandwell et al. (2014) grided with 500 m cell size. The use of regional data was necessary to extend profiles 14 and 15 beyond the surveyed seismic lines to reduce the edge effects in the models.

Merging the marine and satellite data into a continuous record was done before gravity modeling. The marine data is collected much closer to the mean sea-level and thus it has higher resolution compared to satellite gravity data, while satellite data offer a better regional trend. These differences are shown in Figure 3.4b and 3.4c.

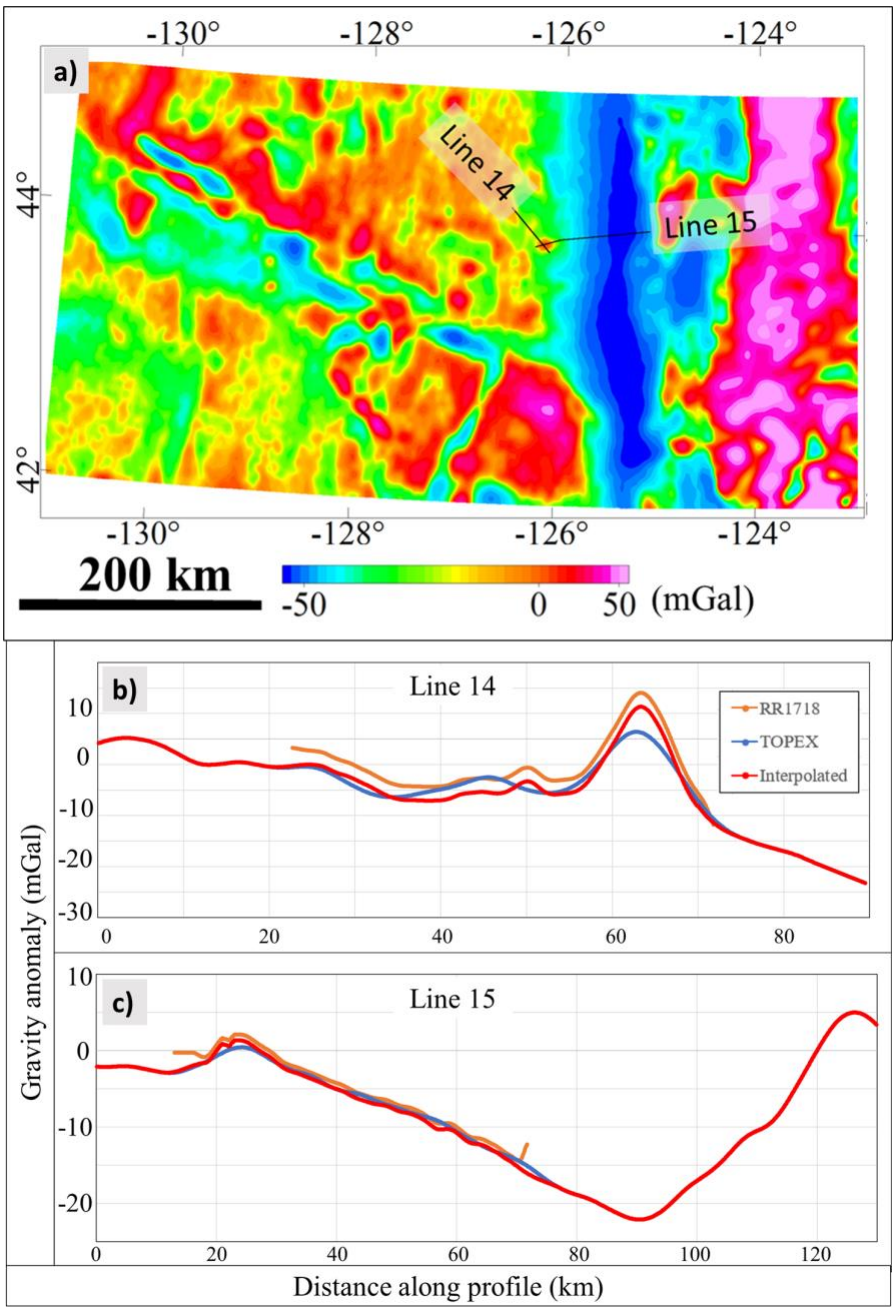

Figure 3.4: a) Regional Free-air gravity anomaly grid from (Sandwell et al., 2014); b) & c) comparison of shipborne (Tominaga, 2017a) and satellite gravity data along with merged anomaly data.

To level two datasets, the average anomaly differences between satellite and marine gravity data were subtracted from marine data (i.e., marine data was shifted to align with satellite data). Still, some mismatches remained at the ends of leveled marine dataset that were removed and then interpolated. Spline interpolation via “interp1d” MATLAB function was used to fill these gaps. The interpolated and merged anomalies along profile line 14 & 15 are shown in Figure 3.4b & c.

3.3 Magnetic anomaly data

Magnetic anomaly data (total intensity after ambient field was removed) was obtained from Bankey et al. (2002) (https://mrdata.usgs.gov/magnetic/) which is shown in Figure 3.55a. This data had 1-km grid spacing with DNAG (Decade of North American Geology) projected coordinate system. It represents the magnetic field at elevation of 305 m above terrain. For keeping both potential fields with the same grid size, it was regirded to 500 m cell size with WGS84/UTM10 projection system. This dataset is a compilation of several surveys that took place at different times with the most recent survey acquired in 2001. So, January 1, 2001 was used as the survey period to calculate the inclination and declination, which were 65° and 18° respectively, and total magnetic field intensity of 52000 nT in the study area. These parameters were used later for magnetic modeling. These values were also used for reduction to the pole (RTP) that was performed on this grid for magnetic isochrone analysis.

This research also incorporated a second set of magnetic anomaly data obtained from the cruise RR1718 (Tominaga, 2017b). The data was collected simultaneously with the marine gravity data using a SeaSpy magnetometer system. However, it is worth noting that only Line 14 was covered during this specific cruise, while Line 15 was not recorded due to a kink in its trajectory that prevents deploying the magnetometer. The surveyed magnetic line 14 is shorter than the model profile 14 similar to the gravity profiles. Therefore, the same merging methodology described in section 3.2 was also applied here. The resulting marine magnetic anomaly profile, as well as the profiles derived from the regional magnetic anomaly and the merged data, are presented in Figure 3.55b.

3.4 Bathymetry data

Bathymetry data from various sources were considered for this study. The evaluated options included data from several publicly available sources (Ryan et al., 2009; Tozer et al., 2019; GEBCO Bathymetric Compilation Group, 2022). Among these, the GMRT 4 dataset from Ryan et al. (2009) offered the highest resolution, as depicted in Figure 1.1, compared to other publicly available datasets. Hence, the GMRT 4 dataset was selected for this study. By default, the dataset has a grid cell size of 39m, which was subsequently regrided to a 50 m spaced grid.

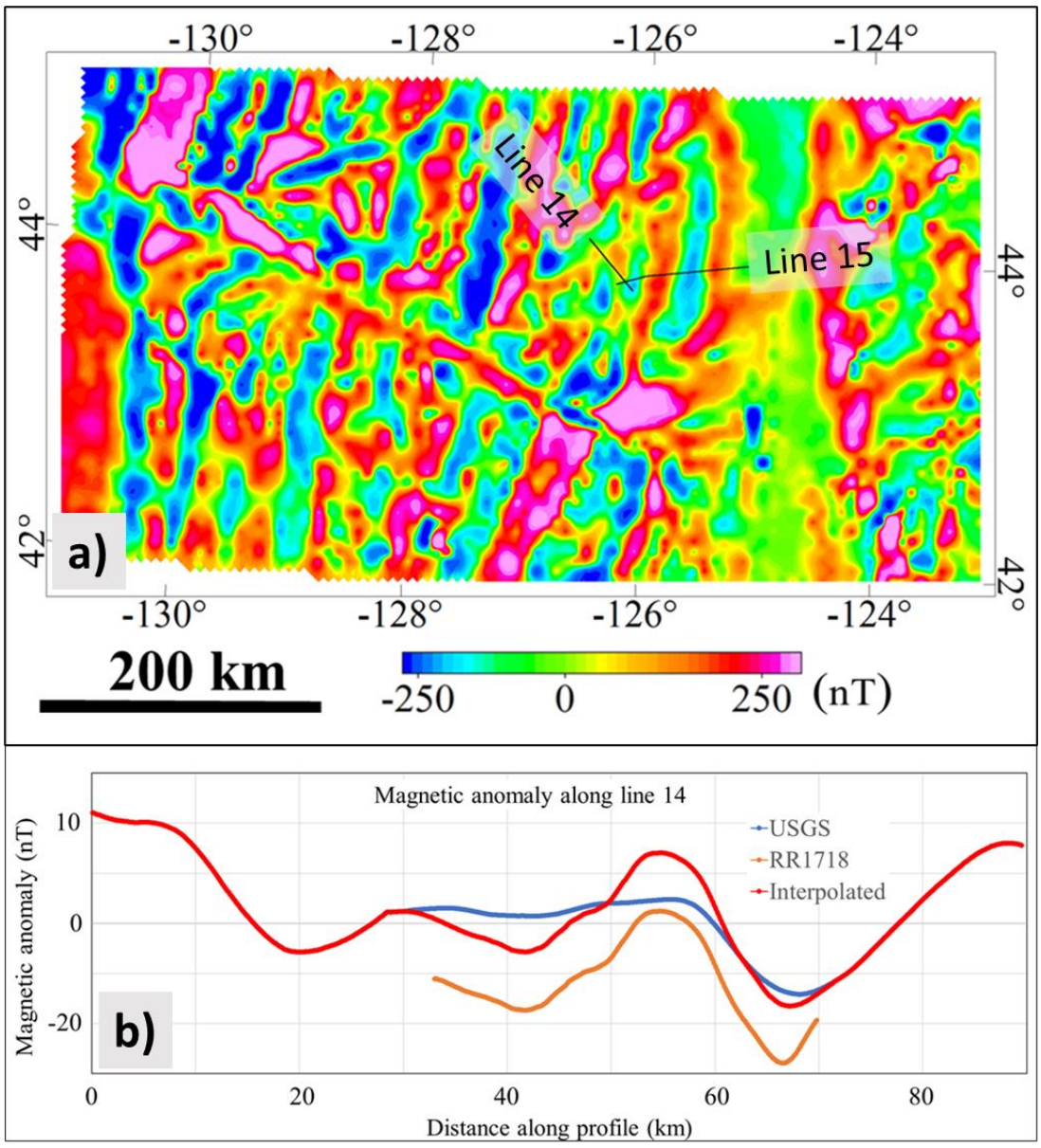

Figure 3.5: a) Regional magnetic anomaly grid from Bankey et al. (2002); b) comparison of shipborne (Tominaga, 2017b) and regional magnetic anomaly data along with merged anomaly data. There are no marine magnetic anomalies recorded for line 15.

3.5 Ocean drilling data

Ocean drilling data, if available, are firsthand sources for P-wave velocity, bulk density, and magnetic susceptibility. However, the closest ocean drilling site to the Diebold Knoll on JdF plate is DSDP-18 site 174 (Deep Sea Drilling Project, 1989), which is ~113 km north of the Diebold Knoll (Figure 2.2). Site 174-A had a maximum penetration of 879 m from seafloor, but it did not penetrate basement that was estimated to be ~30 m beneath the well at a depth of 911 m (Figure 3.6).

The total sedimentary section penetrated at site 174-A can be broadly divided into two units (Kulm et al., 1973). Unit 1 is predominantly composed of medium to very fine turbidite sand layers fining upward to silt or silty clay (yellow color in Figure 3.6). As this site is located in the distal part of the Astoria Fan, Unit 1 (0-284mbsf, Figure 3.66) was interpreted as Astoria Fan deposit. Unit 2 (284-879 mbsf) is an Abyssal plain deposit which consists of Upper Pleistocene to Pliocene basal silt grading upward to silty clay. Although the boundary between these two layers is very pronounced on seismic reflection and detected in lithology, there is no indication that the discontinuity is erosional or a major break in depositional history (Kulm et al., 1973).

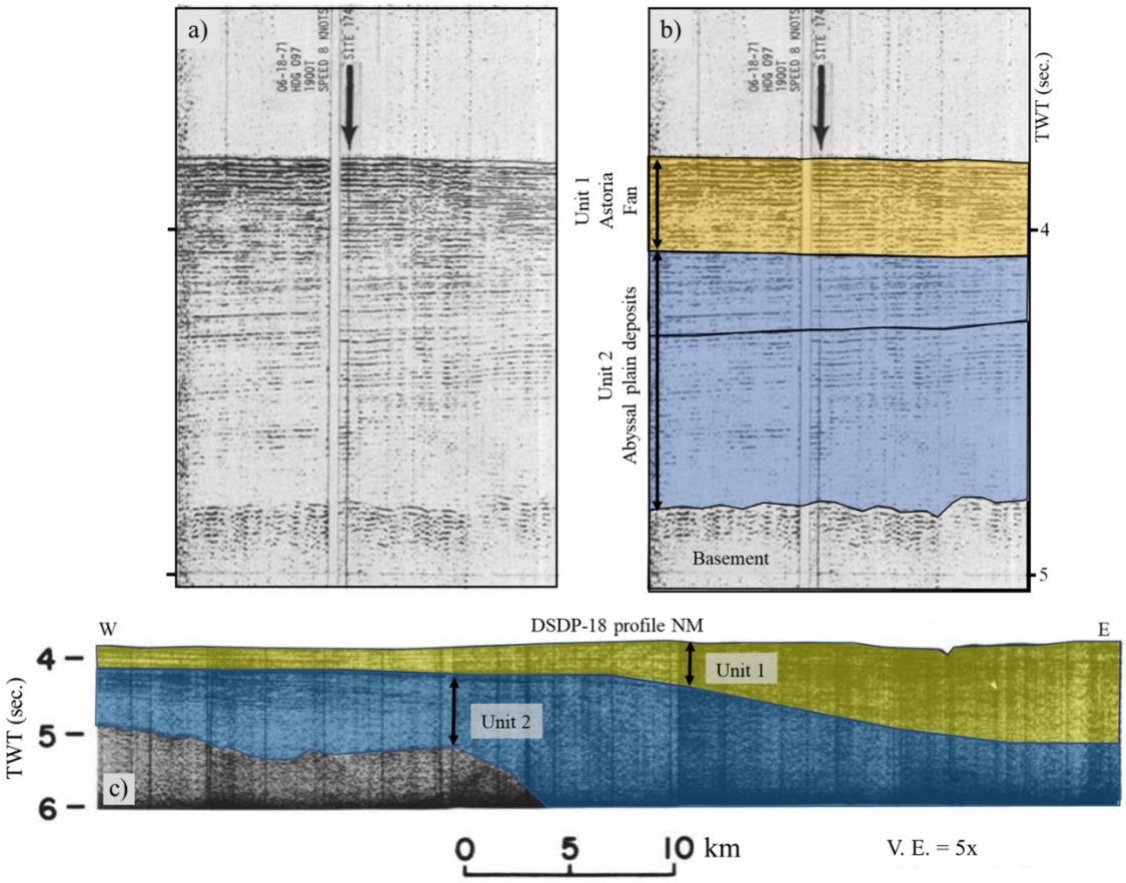

Figure 3.6: Seismic profiles over DSDP-18 site 174 adopted from (Kulm et al., 1973). a) is uninterpreted and b) interpreted seismic section over the DSDP-18-174 according to the DSDP report. Unit 1 is more or less horizontal, whereas parallel reflectors in Unit 2 are inclined toward the subduction zone. Notice that there is no indication of lateral direction in the original image, but based on inclination of unit 2, it can be inferred that the left part of the image is toward east. c) West-East seismic profile ~30 km south of the drill site. Units 1 and 2 in this image were not interpreted in the original publication; they were projected from the drill site seismic image.

Bulk density from the core logs and most importantly age of the sediments are two other sets of information that were used in this study. Summary of density and age from DSDP-18 site 174-A is provided in Table 2.

Table 2: Summary of density and age from DSDP-18-174-A.

	Average	Minimum	Maximum
Wet bulk density (g/cm^3)	1.87	1.32	2.23
Age (million year)			
Depth of section (mbsf)	Minimum	Maximum	(Deep Sea Drilling Project, 1989)
28 to 417.5	0.011	1.8 (Pleistocene)	
446 to 778.5	1.8	5 (Pliocene)	

ODP-146 and ODP-204 also partially took place near the Diebold Knoll, but both were on the accretionary prism (Westbrook et al., 1994; Trehu et al., 2006). As a result, both were unusable for this study.

Chapter - 4: Methodology

4.1 2.75D Geophysical modeling

The integrated geophysical models were developed using Oasis Montaj GM-SYS. At first, a skeleton model with several layers at different depths was built by utilizing topography/bathymetry and seismic studies. The program extends the horizontal length to infinity (in reality ±30000 km) along the profile to eliminate edge effects. GM-SYS also extracts gravity and magnetic anomaly values along the profiles.

Each subsurface layer in the model can be subdivided into a number of blocks. Each block is assigned physical properties, namely density and magnetic susceptibility. GM-SYS utilizes methods and algorithms described in Talwani et al. (1959), Talwani and Heirtzler (1964), Rasmissen and Pedersen (1979), Won and Bevis (1987) to calculate the gravity and magnetic anomalies for this initial model. Three variables, namely density, magnetic susceptibility, and layer geometry, can be adjusted to ensure that the calculated gravity and magnetic anomalies align with the observed anomalies. However, some of those parameters cannot be modified as they are constrained by seismic and scientific drilling results.

Instead of using typical 2D model, this study used 2.75D modeling approach which is available in the Geosoft Oasis Montaj – GM-SYS software (**Error! Reference source not found.**).

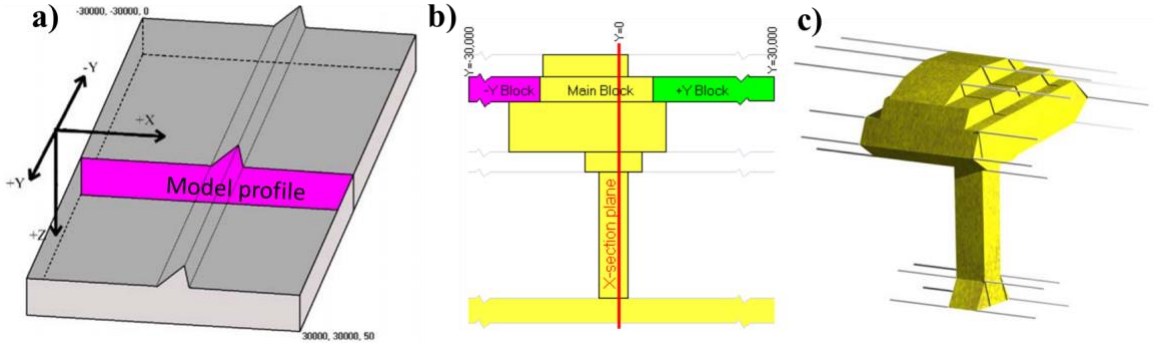

Figure 4.1: a) A typical 2D profile; b) and c) illustration of 2.75D showing blocks within the section and different extents for each block. Figures from Northwest Geophysical Associates Inc., (2004).

2.75D models have greater flexibility than 2D models in terms of modeling for local features (like seamounts) which asymmetrically extends across either side of a model profile.

Two integrated geophysical models, line 14 & line 15, were developed for this study (locations of these profiles are shown in Figure 1.1). For these models, the subsurface was divided into several layers that included water, sediments (several layers), crust (upper and lower) and mantle.

Thickness, density and magnetic susceptibility values were gathered from several sources which are listed below in Table 3. The following constraints were assumed for the models:

Water: The water density value of 1.03 g/cm^3 and zero magnetic susceptibility were assumed (Telford et al., 1990). The thickness of the water column was determined from bathymetry data (section 3.4) and was fixed during modeling.

Sediments: Sedimentary layers were assigned densities ranging from 2.0 g/cm^3 (top layer) to 2.65 g/cm^3 (bottom layer near the subduction zone) following the study of Ashraf (2021). Zero magnetic susceptibility value was assigned to all sediments.

Oceanic crust: Unlike many crustal gravity models that treat the oceanic crust as a single unit, this study divides it into distinct upper and lower crust (oceanic layers II and III). This division enhances the accuracy of the models by accounting for significant variations in physical properties, especially density, between these layers. Density values for the upper and lower crust were derived using velocity-to-density conversion. Research on the JdF plate's velocity structure near the Diebold Knoll provided valuable insights P-wave velocity studies of JdF (Trehu et al., 1994; Gerdom et al., 2000; Horning et al., 2016; Canales et al., 2017). The initial model was assigned densities of 2.6 g/cm^3 and 2.90 g/cm^3 to the upper and lower crust, respectively.

The magnetic susceptibility of the Juan de Fuca plate is not uniformly distributed and can vary based on depth, location, and composition. Studies have reported varying magnetic susceptibility values for specific regions and depths within the plate. For instance, Horning et al. (2016) observed values ranging from 1,000 to 10,000 μcgs units in the upper crust, while Schouten et al. (2018) reported values between 1,000 and 5,000 μcgs units in the gabbroic lower crust. A single value (+/-2,000 μcgs as in Ashraf, 2021) for both the upper and lower crust was assumed due to limited published research differentiating magnetism between these layers. In addition, crustal layers were divided into normally and reversely magnetized blocks in order to model magnetic anomalies.

The upper crust (Oceanic layer 2) had an average thickness of approximately 2 km, while the lower crust was around 4 km thick (see Table 3).

Mantle: The mantle was assigned a density of 3.3 g/cm^3 and zero magnetic susceptibility (Telford et al., 1990).

Once a satisfactory match is achieved with geologically plausible parameters, the model represents the subsurface structure. It must be noted here that not all parameters can be changed as many of them are constrained with drilling, seismic and/or laboratory measurements. Therefore, at each iteration, a careful evaluation was performed of each model parameter to ensure that adjustment does not violate a priori constraints or geologic reasoning. This process is illustrated in Figure 4.2 as a flow chart of different steps for making an integrated 2.75D model.

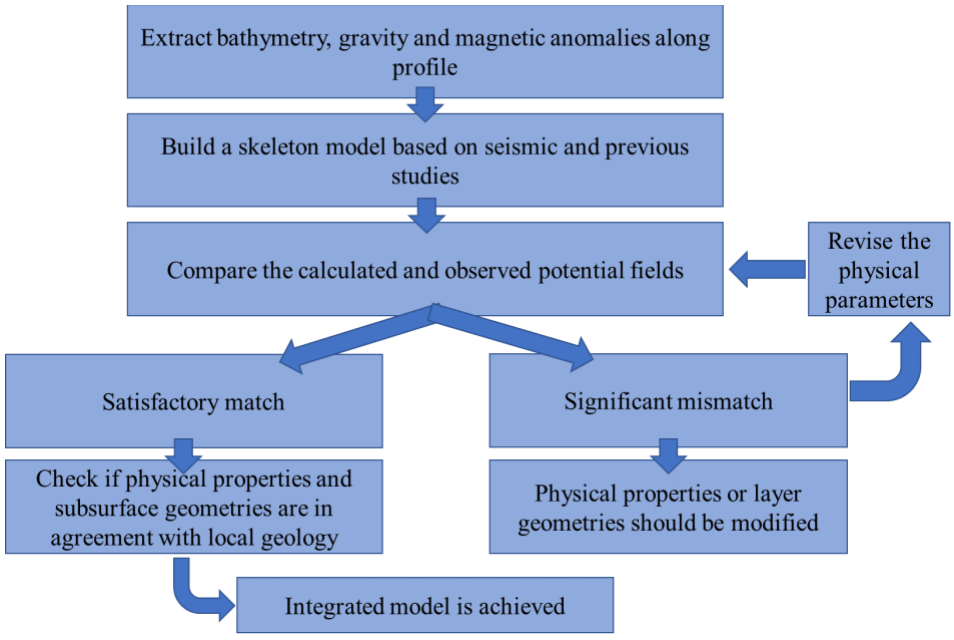

Figure 4.2: Simplified workflow for developing an integrated geophysical model.

4.2 Geological constrains

a) Sedimentary layers near the Diebold Knoll:

Seismic reflection profiles (line 14 and 15) were analyzed for recognizing seismic reflections that represent boundaries between different depositional units. Cross-cutting relationships and onlapping between these sequences and the seamount were also evaluated (Figure 4.3). Sequences that are lying flat surrounding the seamount are interpreted to be deposited after the seamount was formed. Sequences that are lapping on (i.e., thrown up by) the seamount are thought to have been deposited before the seamount and were distorted as the seamount was forming. Seismic sequences from DSDP-18-174 (Figure 3.6) were correlated based on reflection characteristics with sequences near the Diebold Knoll. In particular, horizontal strata on top were interpreted as Unit 1 (Astoria Fan deposits) and inclined strata beneath as Unit 2 (Abyssal plain deposits).

a) Physical properties

Density, magnetic susceptibility, and crustal thickness values were gathered from previous research on the Juan de Fuca plate and Cascadia Subduction Zone (Table 3). As there was no direct information about physical properties and crustal structures of the Diebold Knoll, these parameters were extrapolated from the nearby studies or lab measurements.

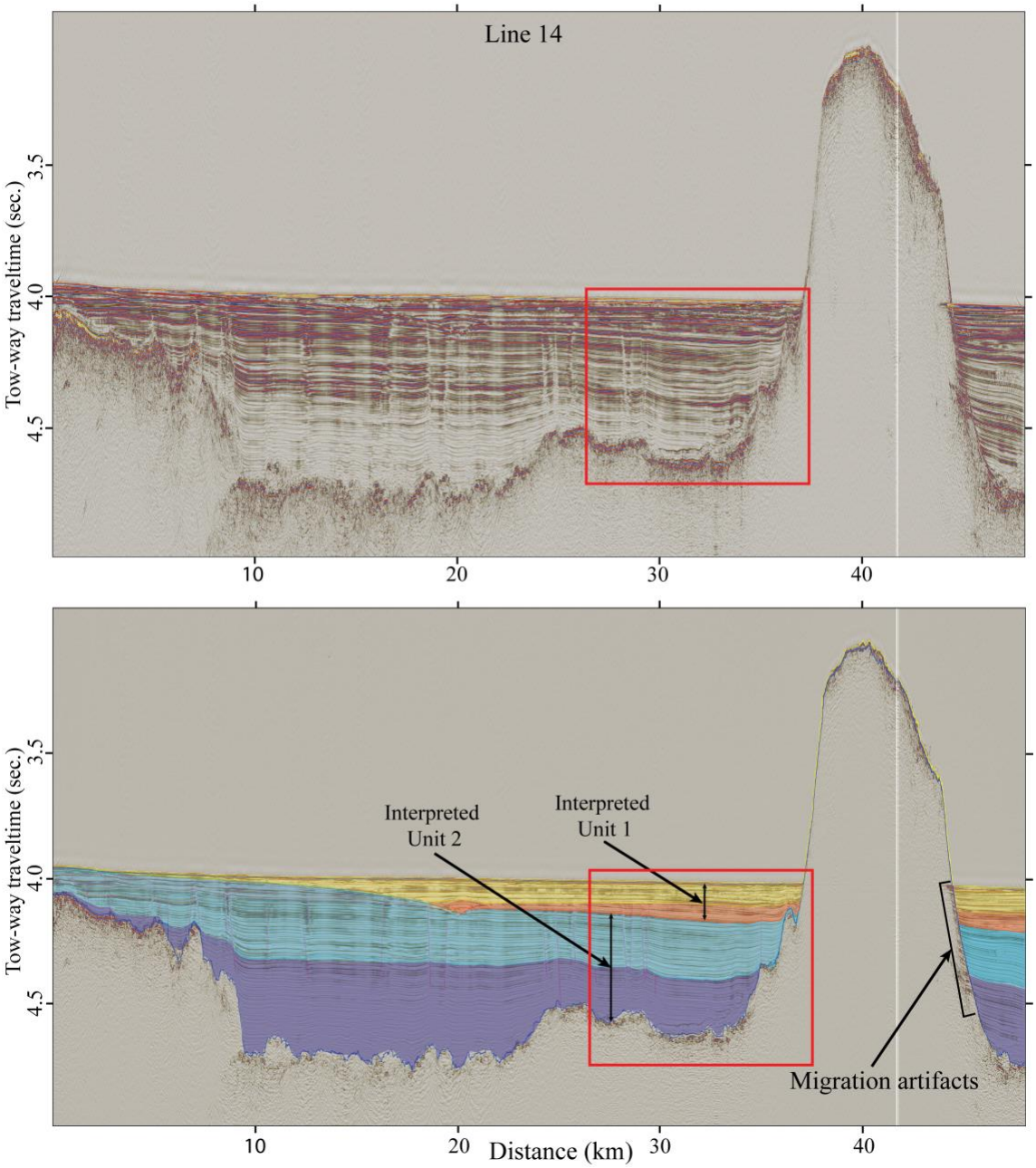

Figure 4.3: 2D MCS data in travel-time. (a) uninterpreted seismic line 14, (b) same profile showing identified sedimentary sequences (profile location shown in Figure 1.1). The red box is the extent of Figure 6.2.

Table 3: Physical properties from previous studies.

Subsurface layers	**Density in g/cm^3 (published value)**	**Magnetic susceptibility (μ-cgs)**	**Thickness in km (published value)**	**Source**
Sediments	2.00-2.45	0	-	(Telford et al., 1990; Horning et al., 2016; Ashraf, 2021)
Oceanic layer 2	2.65	±2000	2	(Carlson and Herrick, 1990; Trehu et al., 1994; Gerdom et al., 2000; Horning et al., 2016)
Oceanic layer 3	2.95	±2000	4.5	
Mantle	3.3	0		(Telford et al., 1990)

4.3 Estimating thickness of crustal root

As seamounts are extra mass on oceanic plates, they tend to develop a root as they become isostatically compensated. Two different ways were used to estimate the root thickness. The first one was based on Airy isostacy, which is a simple way to calculate the change in crustal thickness due to adding a mass on lithospheric plates (Airy, 1855).Click or tap here to enter text. The idea is that the sum of the product of density and thickness for all layers above an assumed compensation depth must be equal for all

isostatically compensated structures (Telford et al., 1990; Lillie, 1998). Isostatic compensation depth was assumed to be 25 km below MSL under the Juan de Fuca plate, as oceanic plates are much thinner than continental plates.

The second way to estimate the root thickness was based on analog seamounts in the study area, where the bending Moho was imaged by seismic reflection (Figure 2.33). The height of that seamount and thickness of the root was used to estimate the root thickness below the Diebold Knoll.

Chapter - 5: Results

5.1 Tectonic history of Diebold Knoll and age approximation

There are two general ways by which the Diebold Knoll may have formed. It could be emplaced on the oceanic crust in the near ridge settings (i.e., just after the crust formed at the Juan de Fuca spreading center, so the seamount is added to young and weak crust), or it could be formed away from the ridge in the intraplate settings (i.e., it was added much later to already established and relatively strong crust). However, due to lack of direct samples, the exact timing of the Diebold Knoll remains unclear - it could have been any time since the crust formed ~7-7.5 Ma which was determined from magnetic chrons (Figure 5.1).

Figure 5.1 shows the magnetic anomalies in the study area. Pronounced north-south trending highs and lows indicate magnetic reversals. The Diebold Knoll is associated with strong negative anomaly (~280 nT), which is apparent in Figure 5.1. The western part of the seamount complex appears to be superimposed on normal polarity chron 3B, indicating that the seamount formed during a period of reverse magnetic polarity. For developing the integrated models in the next section, the chrons outlined in Figure 5.1 were used to constrain the boundaries between the normal and reversely polarized blocks of the JdF crust.

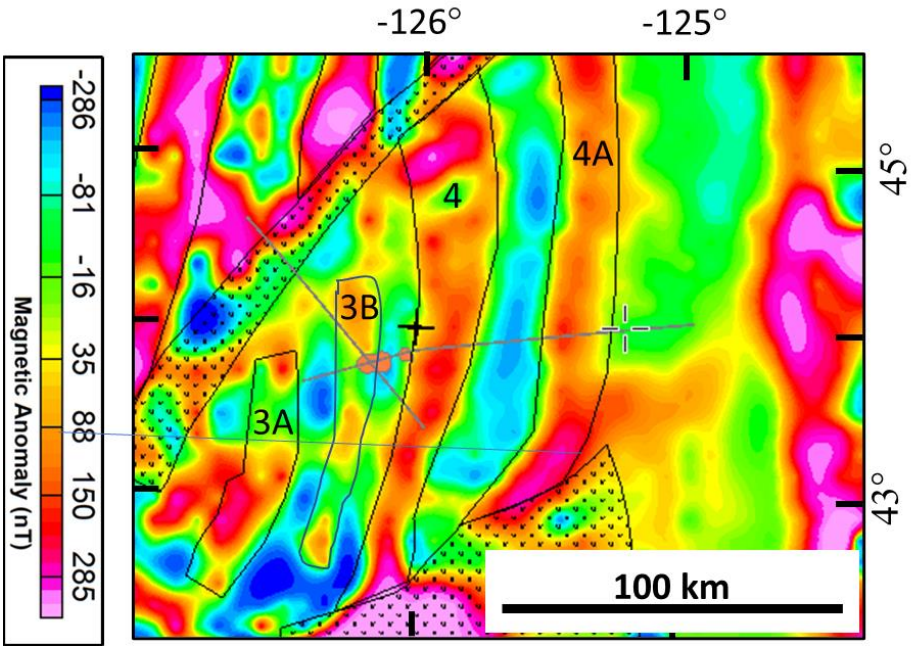

Figure 5.1: Magnetic anomaly around the Diebold Knoll (in orange polygons) from Bankey et al. (2002) along with location of 2D profiles in grey lines and magnetic chrons 3A to 4A shown as thin black polygons from Wilson (2002).

5.2 2.75D integrated models and physical properties

Several integrated models were developed for line 14 and line 15, utilizing various geophysical datasets such as seismic reflection and refraction, gravity and magnetic anomalies, and ocean drilling data. These models were developed to examine three different geological scenarios, which are outlined below and will be further discussed in the following chapter.

5.2.1 Scenario 1: Stable oceanic crust, flat Moho beneath Diebold Knoll with no crustal bending

This scenario assumes no root beneath the seamount complex (i.e., flat Moho). Initial gravity and magnetic anomalies were calculated using the parameters listed in Table 3. However, the density and magnetic susceptibility of the top of the seamount complex (exposed above the basement, shown in light pink color in Figure 5.2a) were adjusted to match the calculated anomalies with the observed gravity and magnetic data for both modelled lines (Figure 5.2aFigure 5.3a)

These models reveal important variations in physical properties within the Diebold Knoll. Specifically, the uppermost part of the knoll, exposed to seawater, exhibits a lower density of 2.6 g/cm^3 compared to the surrounding oceanic layer 2 with a density of 2.65 g/cm^3. The choice of density value of 2.6 g/cm^3 within the seamount for the final model is justified in Figure 5.2b. Density values of 2.55, 2.60 and 2.65 g/cm^3 were evaluated for this sensitivity test. Although all the values produced similar shapes of anomalies, the density value of 2.60 g/cm^3 resulted in the best match in amplitude with observed gravity anomalies (Figure 5.3b).

Additionally, the uppermost part of the knoll shows a significantly lower magnetic susceptibility of 100 micro-cgs compared to the surrounding upper crust with a magnetic susceptibility of 1500 micro-cgs. This is lower than the magnetic susceptibility used for plate scale models in Ashraf (2021) which was +/- 2000 micro-cgs. Because the models

developed in this study are much shorter than models from Ashraf (2021), this magnetic property value fits better the local observed magnetic anomaly.

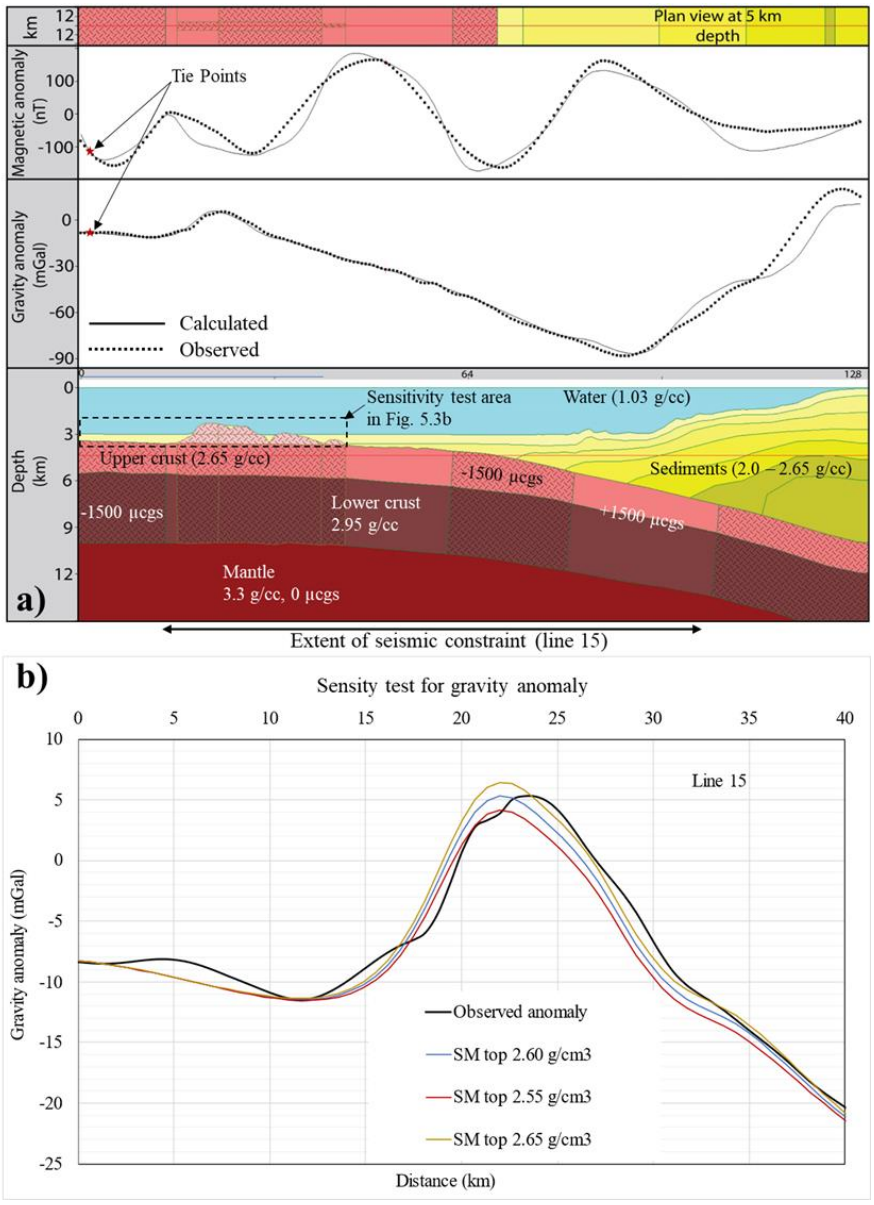

Figure 5.2: a) Integrated geophysical model (bottom section) along profile line 15 (a plain view at 5 km depth is in the top panel). Density of the seamount and sedimentary units are listed in Table 4. b) Sensitivity test for calculated gravity anomaly using different densities for the blocks within the seamount. The value of 2.60 g/cm^3 represented by blue line has the best fit among all other tested density values.

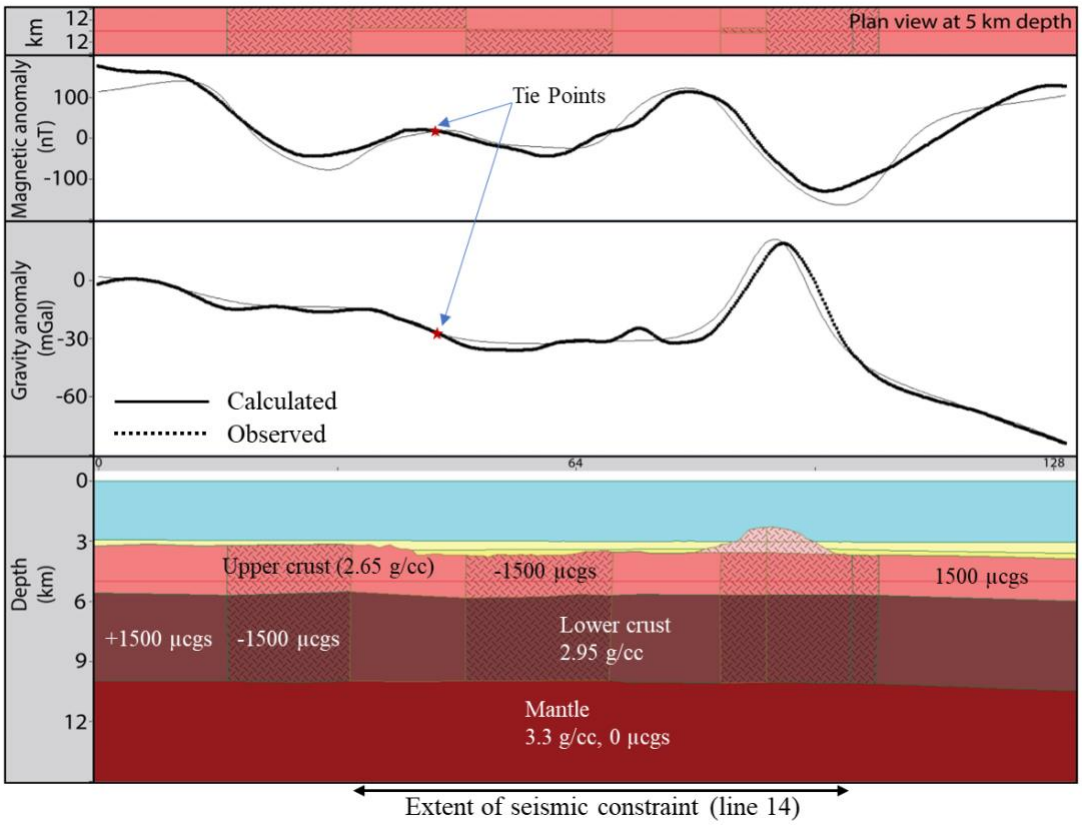

Figure 5.3: 2.75D crustal model along profile line 14 using the same parameters as for line 15 in Figure 5.2a. Density of the seamount and sedimentary units are listed in Table 4.

The derived lower density and magnetic susceptibility values in the uppermost part of the knoll may be attributed to factors such as exposure to seawater, faulting, and hydration.

It is important to note that there is a significant misfit between observed and calculated potential fields in the eastern end of profile 15 over the accretionary prism. This can be attributed to lack of direct physical constraints for modeling in that area, primarily density and depth of the deeper sediments (basement is not well-imaged in seismic data). Therefore, there was no attempt to obtain a better fit in that area.

The lowered properties over the seamount align well with previous studies that have reported similar variations in physical properties in other seamounts and submarine structures exposed to seawater (Kopp et al., 2004; Caratori Tontini et al., 2016; Horning et al., 2016; Lee et al., 2022).

Table 4: Physical properties resulting from integrated models.

Subsurface layers	**Density (g/cm^3)**	**Magnetic susceptibility (μ-cgs)**	**Thickness (km)**
Water	1.03	0	
Sediments	2.1-2.65	0	0.5 - 2
Oceanic layer 2	2.65	±1500	2
Oceanic layer 3	2.95	±1500	4.5
Seamount complex	2.6 - 2.95	-100 to ±1500	
Mantle	3.3	0	

Table 4 provides a summary of the integrated model's physical properties that best fit the given scenario. Another noteworthy observation is that the seamount exhibits reverse magnetization, whereas the majority of the surrounding oceanic crust displays normal magnetization. This is required to match the magnetic anomaly because right above the

seamount there is a negative magnetic anomaly which is accompanied by a pronounced positive anomaly very close to it. It is not possible to match the observed magnetic signature if the seamount is normally magnetized.

5.2.2 Scenario 2: Isostatically compensated seamount

In this scenario, the seamount was assumed to be in complete isostatic compensation. The root thickness was calculated using Airy isostacy model (method described in section 4.30) assuming physical properties listed in Table 4. This results in a 2.75 km thick root (Figure 5.4) and consequently about 10.5 mGal mismatch between calculated and observed gravity anomalies. But the magnetic anomaly is not much affected.

In order to reconcile the gravity anomalies, this model requires an unusually high density (~3.0 g/cm^3) for the top of the seamount complex, which consequently impacts the thickness of its root. This creates a trade-off situation when either the observed gravity field is matched using anomalously high-density value for extrusive igneous rocks (which is not supported by existing literature), or a significant gravity anomaly mismatch which arises due to a thick root in the model.

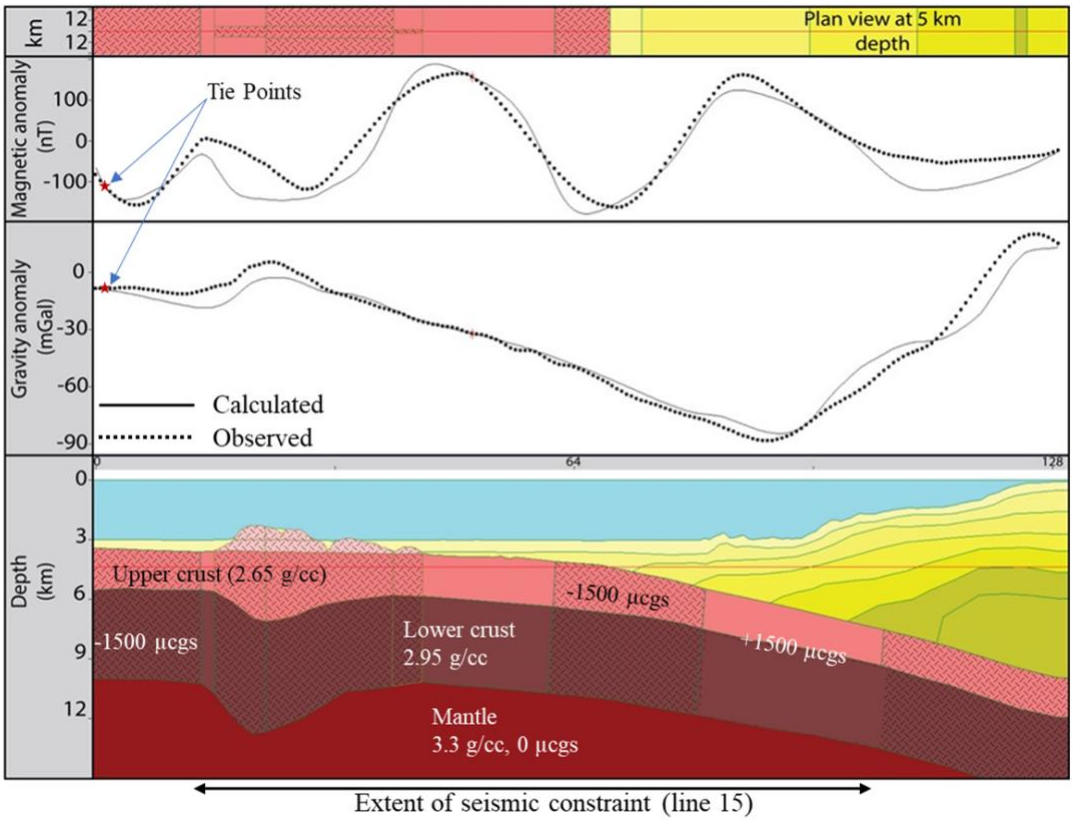

Figure 5.4: Alternative model along line 15 considering isostatic compensation. All other properties other than the thickness of the crust beneath the Diebold Knoll were kept the same.

5.2.3 Scenario 3: Root thickness from analogous regional examples

In this scenario, the root thickness beneath the Diebold Knoll was estimated based on the analysis of analog seamounts located on the Juan de Fuca plate and surveyed during two seismic cruises, as discussed in section 2.3. The computed seamount height-to-root ratio of 0.65 was adopted for the Diebold Knoll, suggesting a root beneath the Diebold Knoll of 0.9 km. Since the crust's bending in this case is not as pronounced as in the second scenario, the calculated gravity anomaly only exhibits up to ~3 mGal misfit when compared to the observed gravity field. Figure 5.5 shows this mismatch which could

potentially be improved by adjusting the Moho boundary within 0.5 km range under the seamount complex or by adding density heterogeneities within the seamount complex. The exact fit for this scenario is intentionally not shown to illustrate uncertainties of the modeling.

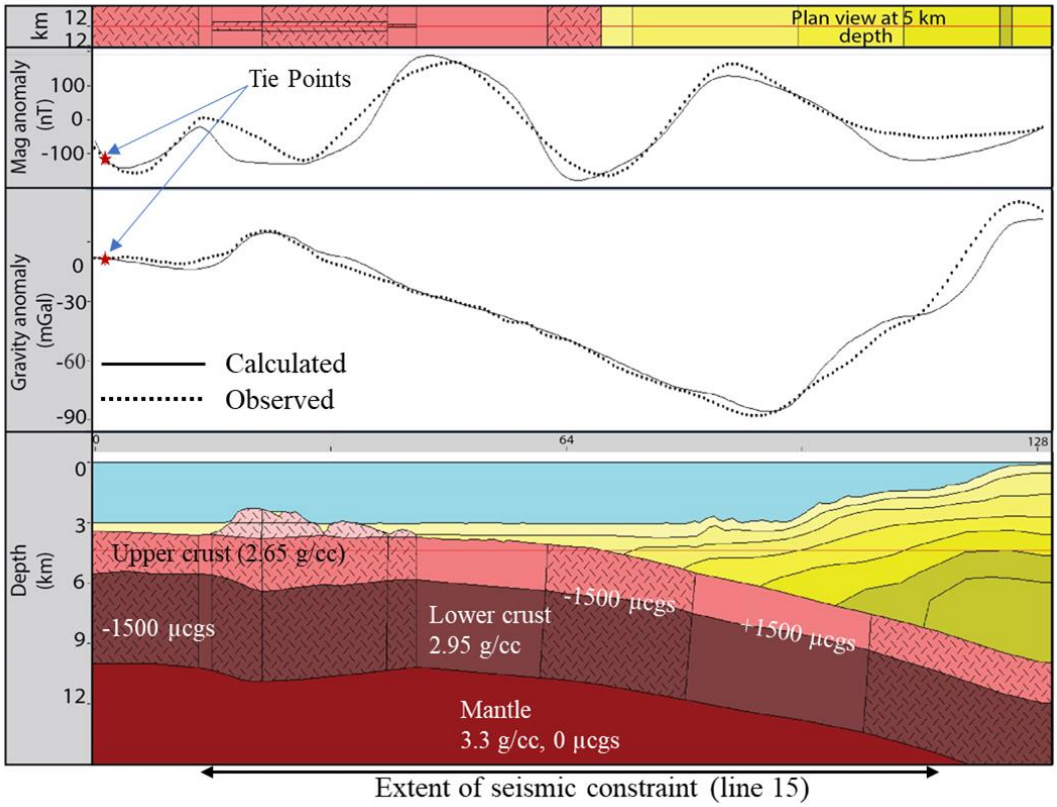

Figure 5.5: Third model scenario where the root beneath the Diebold Knoll is estimated based on the example of seamount PD11/MCS03. Physical properties were kept the same as previous models.

This scenario indicates that if the Diebold Knoll possesses a root, its thickness is about 1 km, and the seamount is not entirely locally compensated or still undergoing compensation. The model in this scenario aligns equally well with the data as scenario 1 (flat Moho).

Chapter - 6: Discussion

6.1 Isostatic compensation of seamounts on the JdF plate

There are numerous isolated seamounts on the Juan de Fuca plate, many of which are buried under sedimentary deposits, particularly near the Cascadia Subduction Zone, where sediments from the Astoria Fan and Nitinat Fan contribute to their burial (Figure 2.2). Seismic surveys MGL1211 and CASIE21 have successfully identified and provided insights into the Moho boundary beneath these submerged seamounts. Among the 16 seamounts/bathymetric highs depicted in Figure 2.2, the Moho is visible under six of them in seismic sections. Notably, only PD11/MCS03 from CASIE21 (Figure 2.3) and L1-SM03 from MGL1211 (located at ~35 km range in Figure 3.2) exhibit apparent roots, while four out of six seamounts with imaged Moho display a relatively flat Moho. On average, seamounts with roots have a root thickness approximately 0.65 times their height (described in section 2.3).

Scenario 1 (Figure 5.2Figure 5.3) assumes a flat Moho beneath the Diebold Knoll, which aligns with the observations of 4 seamounts in Figure 2.2. This scenario also assumes a relatively strong crust that remains undeformed upon the addition of the seamount. Consequently, it suggests that the seamount is relatively younger than the hosting crust (i.e., crust had time to strengthen before the seamount was added) and/or the seamount has not undergone sufficient isostatic compensation yet. This scenario excludes the possibility of the seamount forming near a ridge (i.e., crust and seamount are about of the same age), and instead suggests intraplate volcanism as the likely mechanism of

formation. These findings are consistent with the fact that Diebold Knoll remains elevated above sediments and is not buried or covered by sediments deposition (Figure 3.1Figure 6.3). Therefore, it is likely that the Diebold Knoll formed relatively recently in order to retain its bathymetric exposure.

Scenario 2 in Figure 5.4 assumes completely isostatically compensated Diebold Knoll. This scenario appears to be highly unlikely because it results in a significant mismatch between the observed and calculated gravity anomalies (~10.5 mGal), as depicted in Figure 5.4. In addition, regional examples of analogous seamounts also do not support this scenario, as the six seamounts with imaged Moho exhibit either flat base of the crust or very thin roots.

Scenario 3 with ~0.9 km root beneath the Diebold Knoll, demonstrates a reasonable match with gravity anomalies (as does scenario 1). This scenario finds support from analogous seamounts within the study area (two out of six seamounts with imaged Moho).

Consequently, scenario 2 can be disregarded as an accurate representation of the crustal architecture beneath the Diebold Knoll. This leaves us with scenario 1 (flat Moho) and scenario 3 (small root thickness of $\leq$1 km) as reasonably representative options for the crustal architecture under the Diebold Knoll.

6.2 Age of the Diebold Knoll

The models and magnetic grid analyses (Figure 5.1Figure 5.2) revealed that the Diebold Knoll is reversely magnetized. The crust on which the knoll resides is estimated to be around 7-7.5 million years old (Figures 1.1 and 5.1). So, the Diebold Knoll is younger than approximately 7 million years. There are seven major instances of magnetic reverse polarity since the formation of the crust in the vicinity of the Diebold Knoll (Figure 6.1). However, magnetic anomaly analysis alone cannot discriminate between those seven potential geological ages of the knoll.

If the Diebold Knoll formed near the spreading center (consistent with scenarios 2 and 3 described above), its age would be similar to that of the surrounding crust. In this case, there are three potential time ranges in the late Miocene to early Pliocene (7 – 4.7 Ma) that could correspond to its origin. On the other hand, if the seamount formed far from the Juan de Fuca ridge on older JdF crust (intraplate volcanism, scenario 1), there are four possible time ranges of reverse magnetic polarity in the mid Pliocene to early Holocene (4.5 – 0.8 Ma). In this scenario, the crust would be relatively strong and stable at the time of the seamount formation (Figure 6.1).**Error! Reference source not found.**

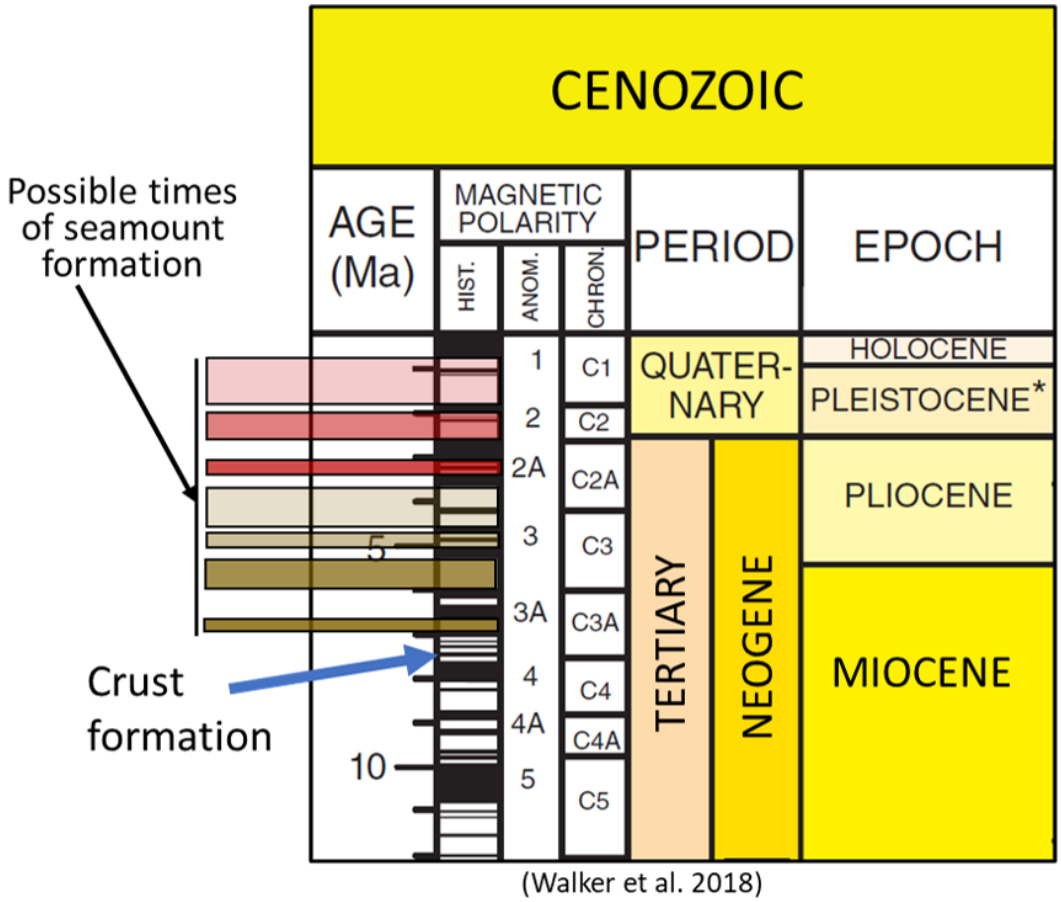

Figure 6.1: Geologic time scale v6 adopted from Walker and Geissman, (2022) showing time windows of negative magnetic anomalies following crust formation, represented by different colors.

The relationship between isostatic compensation, the age of oceanic crust, and the 2.75D models can help narrow down the time of origin for the Diebold Knoll between these two possibilities (i.e., older vs younger seamount age). Seamounts formed on young crust near spreading ridges are associated with thin effective elastic lithospheric thickness (Watts and Ribe, 1984; Kellogg et al., 1987), while those formed on older crust exhibit a higher degree of local isostatic equilibrium (Kellogg et al., 1987).

Due to the significant mismatch between observed and calculated gravity and magnetic anomalies in scenario 2 and analogous examples from the JdF plate, it can be concluded that the Diebold Knoll is not in complete local isostatic equilibrium. This suggests that the seamount was emplaced on relatively older crust and eliminates three Miocene to early Pliocene formation options. However, the exact age of the seamount cannot be definitively determined based on these assumptions. Nonetheless, in scenario 1, where no crustal bending is required, it is suggested that the seamount formed on relatively old crust. This implies that the last three reverse magnetic anomalies (0.8-1.8 Ma, 2-2.6 Ma, 3-3.3 Ma; Figure 6.1) are the most plausible time ranges for the origin of the Diebold Knoll. The oldest reversed chron out of these three may be even plausible for scenario 3, as the seamount is assumed to have a very thin root.

One additional constraint that can provide further validation for the seamount's age is the cross-cutting relationship between the sedimentary sequences and the igneous body of the seamount, which is illustrated in Figure 6.2Figure 6.3.

Based on lithology and seismic reflection data from DSDP-18-174A (Figure 3.6), the top unit (Unit 1) was clearly identified by (Kulm et al., 1973). This unit was deposited as part of the Astoria Fan, with sediment primarily originating from the Colombia River (Kulm et al., 1973; von Huene and Kulm, 1973; Prytulak et al., 2006). The lower Unit 2 consists of abyssal plain deposits, which exhibit bending along with the JdF plate as it enters the subduction zone (Figure 3.6c). Details regarding these units are discussed in section 3.5.

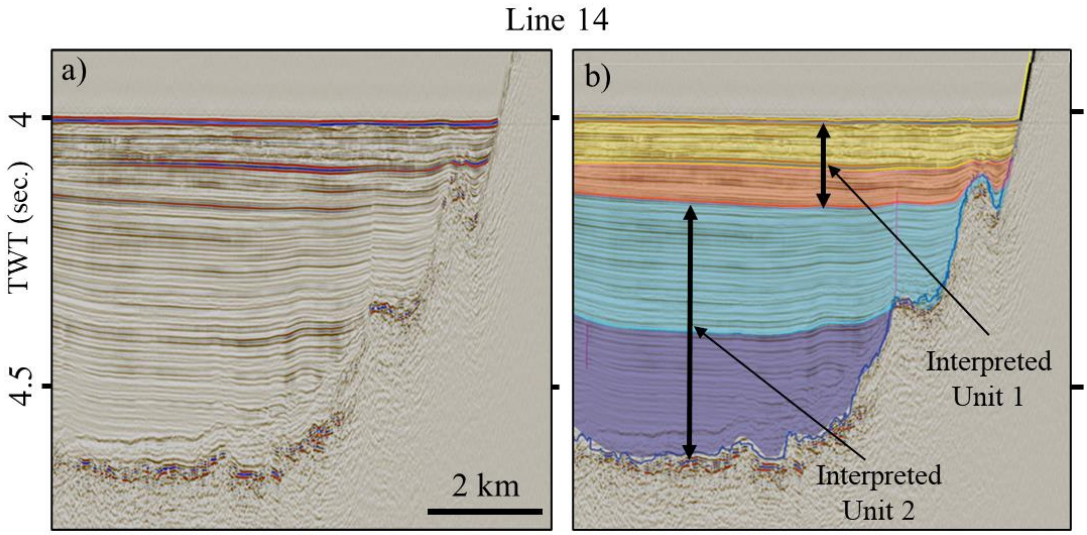

Figure 6.2: Zoomed in portion of line 14 showing sedimentary deposit NW to the Diebold Knoll. The extent of this figure is shown in Figure 4.3. Sedimentary sequences of Unit 2 and lower portion of Unit 1 are lapping onto the seamount suggesting that they were deposited before the Diebold Knoll.

Similar depositional sequences are observed near the Diebold Knoll, as seen in line 14 and 15 (Figure 6.2Figure 6.3). The top two sequences exhibit relatively flat characteristics and resemble Unit 1 identified in the DSDP-18 seismic profiles, while the remaining sequences show similarities with Unit 2. Additionally, interpreted Unit 2 or Abyssal plain deposits as well as lower part of Unit 1 are lapping onto the body of the Diebold seamount complex (Figure 6.2Figure 6.3) suggesting that they are older than the Diebold Knoll. In addition, the smallest peak in this seamount complex (easternmost peak covered by sediments in line 15, Figure 6.3) breaks through the lower part of the interpreted Unit 2, but the upper part of this unit and lower part of Unit 1 (orange layer in Figure 6.3) exhibit a characteristic upward bending.

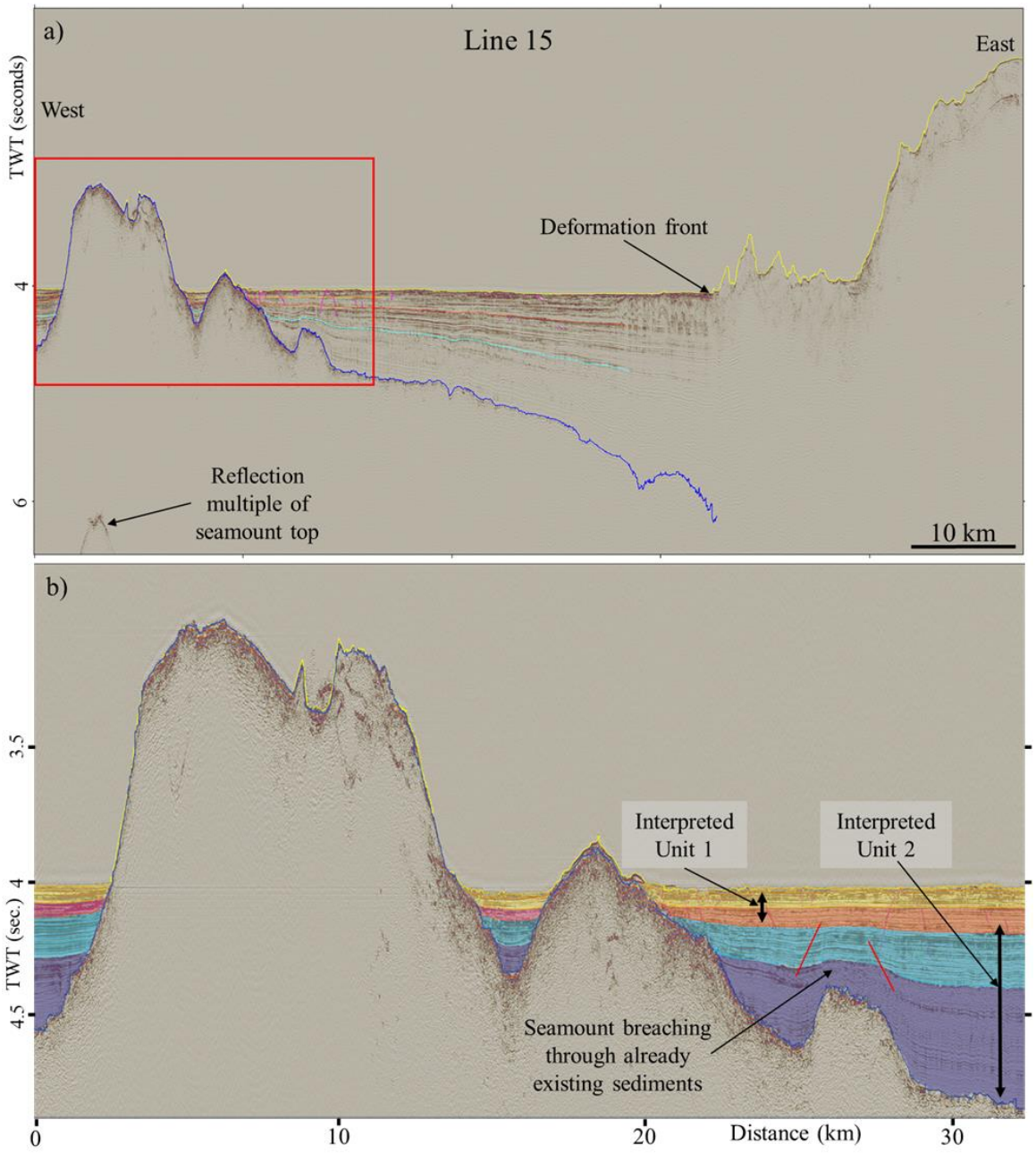

Figure 6.3: a) Uninterpreted line 15 (location on Figure 1.1 and extent on Figure 5.2) showing deformation front toward east and subducting JdF plate. b) Sequences interpreted and correlated with DSDP-18 site 174 seismic units.

This indicates these units were already in place when the volcanic seamount came through, i.e., these layers are older than the seamount. Notably, the top of Unit 1 or Astoria Fan deposits (yellow layer in Figure 6.3) lie flat to the seamount body, meaning that this unit was deposited after the seamount formation.

The contact between Unit 1 and Unit 2 marks the time after which the seamount was emplaced. However, this interface is not a hiatus or not an erosional discontinuity (Kulm et al., 1973; Prytulak et al., 2006). That means the seamount formed when the depositional environment was already shifted from Abyssal pain to Astoria Fan deposits, and the seamount formed sometimes during the deposition of Unit 1.The maximum age of sedimentary rocks at ~900 m at nearby DSDP-18-174A was 5 million years (Table 2). The thickness of sedimentary deposits around the Diebold Knoll is ~600 m and it is ~103 km further away from the Astoria Fan, so the thickness of the Astoria Fan deposits (Unit 1) at the Diebold Knoll will be thinner than at the DSDP site.

The disturbed sedimentary layers and cross-cutting relationships with the seamount suggest that the Diebold Knoll formed after the interface between Units 1 and 2. Based on geochemical analysis of depositional sequences in the Northern CSZ, Bjornstad et al. (2001) and Prytulak et al. (2006) suggested that the change in depositional environment happened at around 2.5 million years ago. Upper 417m on DSDP-18 site 174A (which includes the discontinuity) is suggested to be 1.8 million years old (Table 2; Deep Sea Drilling Project, 1989).

DSDP data and magnetic anomalies narrow down the time of formation to the latest possible time window, i.e., 0.8-1.8 Ma. However, it is worth noting that direct correlation of seismic profile 14 and 15 and the DSDP-18-174 was not possible as the DSDP site is more than 100 km away from the Diebold Knoll. Despite that, the interpreted age range of the Diebold Knoll is confident as it is supported by cross-cutting relationship and magnetic signature.

6.3 Physical properties of the Diebold Knoll:

The 2.75D models showed that the top portion of the Diebold Knoll has relatively lower density and magnetic susceptibility values compared to the surrounding upper crust. The density of the portion of the seamount above basement is 0.05 g/cm^3 lower than the upper crust. This variation seems to be insignificant but due to its proximity to the surface, a very small change in the density has greater effect on the calculated gravity anomalies. The exposed part of the Diebold Knoll to the seawater is almost non-magnetic with only -100 µcgs magnetic susceptibility. Thus, the effect of reduced magnetic properties (100 µcgs vs 1500 µcgs) is much more pronounced than variations in density.

Velocity analysis of seismic reflection profiles from CASIE21 supports this interpretation (Figure 2.3). They found that there is a pronounced decrease in velocity gradient within the upper part of the seamount (Lee et al., 2022). This lower density, magnetic susceptibility, and lower seismic P-wave velocity (Hammer et al., 1994; Weigel and Grevemeyer, 1999; Watts et al., 2021; Lee et al., 2022) is interpreted to be result of

faulting and hydration of the Diebold Knoll during or after its formation. This processes are documented on the JdF plate and are attributed to subduction related bending (Nedimović et al., 2009).

Chapter - 7: Conclusions

Integrating multiple geophysical datasets over the Diebold Knoll on the Juan de Fuca plate has allowed to model the crustal architecture beneath that feature and determine heterogeneity of physical properties associated with its formation. The incorporation of different datasets has helped to establish a geologically representative tectonic history of this seamount, despite the lack of a direct method for age dating. The primary findings of this study are summarized below:

Toward **Objective 1** (Physical properties and crustal architecture of Diebold Knoll):

The uppermost part of the Diebold Knoll that is exposed above the basement has an average density of 2.6 g/cm^3, which is 0.05 g/cm^3 lower than the surrounding upper crust of the Juan de Fuca plate. This portion of the seamount complex is also characterized by a very low magnetic susceptibility (only 100 µcgs vs 1500 µcgs for the rest of the crust). The lower density and magnetic susceptibility within the top of the seamount are interpreted to be evidence of faulting and hydration during and/or after the formation of the seamount. The modeling suggests that the rest of the seamount complex has the same densities and magnetic susceptibilities as the host oceanic crust. The seamount has either a flat Moho beneath it or a very thin (≤1 km) crustal root and it is not completely isostatically compensated.

Toward **Objective 2** (tectonic history of Diebold Knoll):

The entire seamount complex is reversely magnetized, suggesting seven potential time intervals for its formation (two in the Miocene, three in the Pliocene and two in the Quaternary). Cross-cutting relationships between the seamount and sedimentary layers, as well as data from the nearest DSDP suggest that the Diebold Knoll formed in an intraplate settings during the Quaternary period, between 0.8-1.8 Ma. To discriminate further, direct sampling of the seamount's rocks (dredging or drilling) is necessary.

The findings of this study, namely the derived physical property variation within the Diebold Knoll, can provide important constraints for future research related to seamount subduction in the CSZ. Additionally, the integrated approach used in this study can be used in other regions to determine crustal structure, physical property variations and age of formation of intraplate seamounts.

References

Abercrombie, R.E., Antolik, M., and Ekström, G., 2003, The June 2000 Mw 7.9 earthquakes south of Sumatra: Deformation in the India–Australia Plate: Journal of Geophysical Research: Solid Earth, v. 108, p. ESE 6-1-ESE 6-16, doi:10.1029/2001JB000674.

Adams, J., 1990, Paleoseismicity of the Cascadia Subduction Zone: Evidence from turbidites off the Oregon-Washington Margin: Tectonics, v. 9, p. 569–583, doi:10.1029/TC009i004p00569.

Adams, J., and Weichert, D., 1994, Near-term probability of the future Cascadia megaquake: US Geol. Surv. Open-File Rept. 94, v. 568.

Airy, G.B., 1855, III. On the computation of the effect of the attraction of mountain-masses, as disturbing the apparent astronomical latitude of stations in geodetic surveys: Philosophical Transactions of the Royal Society of London, v. 145, p. 101–104, doi:10.1098/RSTL.1855.0003.

Ashraf, A., 2021, Geological Structures and Crustal Architecture of the Cascadia Subduction Zone from the Integration of Multiple Geophysical Datasets: University of Nebraska-Lincoln, doi:https://digitalcommons.unl.edu/geoscidiss/135.

Atwater, B.F., 1987, Evidence for Great Holocene Earthquakes Along the Outer Coast of Washington State: Science, v. 236, p. 942–944, doi:10.1126/SCIENCE.236.4804.942.

Atwater, T., 1989, Plate tectonic history of the northeast Pacific and western North America: The Eastern Pacific Ocean and Hawaii, p. 21–72, doi:10.1130/DNAG-GNA-N.21.

Atwater, B.F., and Hemphill-Haley, E., 1997, Recurrence intervals for great earthquakes of the past 3,500 years at northeastern Willapa Bay, Washington: Professional Paper, doi:10.3133/PP1576.

Atwater, B.F., Musumi-Rokkaku, S., Satake, K., Tsuji, Y., Ueda, K., and Yamaguchi, D.K., 2015, The orphan tsunami of 1700—Japanese clues to a parent earthquake in North America:, doi:https://doi.org/10.3133/pp1707.

Audet, P., Bostock, M.G., Boyarko, D.C., Brudzinski, M.R., and Allen, R.M., 2010, Slab morphology in the Cascadia fore arc and its relation to episodic tremor and slip: Journal of Geophysical Research: Solid Earth, v. 115, p. 0–16, doi:10.1029/2008JB006053.

Bankey, V. et al., 2002, Digital data grids for the magnetic anomaly map of North America: Open-File Report, doi:10.3133/OFR02414.

Bell, R., Sutherland, R., Barker, D.H.N., Henrys, S., Bannister, S., Wallace, L., and Beavan, J., 2010, Seismic reflection character of the Hikurangi subduction interface, New Zealand, in the region of repeated Gisborne slow slip events: Geophysical Journal International, v. 180, p. 34–48, doi:10.1111/j.1365-246X.2009.04401.x.

Bilek, S.L., Schwartz, S.Y., and DeShon, H.R., 2003, Control of seafloor roughness on earthquake rupture behavior: Geology, v. 31, p. 455–458, doi:10.1130/0091-7613(2003)031<0455:COSROE>2.0.CO;2.

Bjornstad, B.N., Fecht, K.R., and Pluhar, C.J., 2001, Long History of Pre-Wisconsin, Ice Age Cataclysmic Floods: Evidence from Southeastern Washington State: The Journal of Geology, v. 109, p. 695–713, doi:10.1086/323190.

Bodmer, M., Toomey, D.R., Hooft, E.E.E., and Schmandt, B., 2018, Buoyant Asthenosphere Beneath Cascadia Influences Megathrust Segmentation: Geophysical Research Letters, v. 45, p. 6954–6962, doi:10.1029/2018GL078700.

Buchs, D.M., Hoernle, K., and Grevemeyer, I., 2016, Seamounts, *in* Encyclopedia of Earth Sciences Series, Springer Netherlands, v. Part 2, p. 754–760, doi:10.1007/978-94-007-6644-0_34-1.

Burgette, R.J., Weldon, R.J., and Schmidt, D.A., 2009, Interseismic uplift rates for western Oregon and along-strike variation in locking on the Cascadia subduction zone: Journal of Geophysical Research: Solid Earth, v. 114, doi:10.1029/2008JB005679.

Burgmann, R., Kogan, M.G., Steblov, G.M., Hilley, G., Levin, V.E., and Apel, E., 2005, Interseismic coupling and asperity distribution along the Kamchatka subduction zone: Journal of Geophysical Research: Solid Earth, v. 110, p. 1–17, doi:10.1029/2005JB003648.

Canales, J.P., Carbotte, S.M., Nedimovic, M.R., and Carton, H., 2017, Dry Juan de Fuca slab revealed by quantification of water entering Cascadia subduction zone: Nature Geoscience, v. 10, p. 864–870, doi:10.1038/NGEO3050.

Carbotte, S., Boston, B., and Han, S., 2022, Multi-Channel Seismic Shot Data from the Cascadia margin acquired during Langseth cruise MGL2104 (2021): IDEA,.

Carlson, R.L., and Herrick, C.N., 1990, Densities and porosities in the oceanic crust and their variations with depth and age: Journal of Geophysical Research, v. 95, p. 9153–9170, doi:10.1029/JB095iB06p09153.

Chadwick, J., 2005, Magmatic effects of the Cobb hot spot on the Juan de Fuca Ridge: Journal of Geophysical Research, v. 110, p. B03101, doi:10.1029/2003JB002767.

Clague, J.J., 1997, Evidence for large earthquakes at the Cascadia subduction zone: Reviews of Geophysics, v. 35, p. 439–460, doi:10.1029/97RG00222.

Cloos, M., Cloos, and Mark, 1992, Thrust-type subduction-zone earthquakes and seamount asperities: A physical model for seismic rupture: Geo, v. 20, p. 601, doi:10.1130/0091-7613(1992)020.

Cohen, J.K., and Stockwell, Jr.J.W., 2021, CWP/SU: Seismic Unix Release No. 44R21: an open source software package for seismic research and processing:

Cummins, P.R., Baba, T., Kodaira, S., and Kaneda, Y., 2002, The 1946 Nankai earthquake and segmentation of the Nankai Trough: Physics of the Earth and Planetary Interiors, v. 132, p. 75–87, doi:10.1016/S0031-9201(02)00045-6.

Das, S., and Watts, A.B., 2009, Effect of Subducting Seafloor Topography on the Rupture Characteristics of Great Subduction Zone Earthquakes (S. Lallemand & F. Funiciello, Eds.): Subduction Zone Geodynamics, p. 103–118.

Deep Sea Drilling Project, 1989, Archive of Core and Site/Hole Data and Photographs from the Deep Sea Drilling Project (DSDP): National Geophysical Data Center, NOAA, doi:doi:10.7289/V54M92G2.

DeMets, C., Gordon, R.G., Argus, D.F., and Stein, S., 1990, Current plate motions: Geophysical Journal International, v. 101, p. 425–478, doi:10.1111/J.1365-246X.1990.TB06579.X.

DiPietro, J.A., 2018, Cascadia Volcanic Arc System: Geology and Landscape Evolution, p. 473–499, doi:10.1016/B978-0-12-811191-8.00019-1.

Dominguez, S., Lallemand, S.E., Malavieille, J., and Von Huene, R., 1998, Upper plate deformation associated with seamount subduction: Tectonophysics, v. 293, p. 207–224, doi:10.1016/S0040-1951(98)00086-9.

Dragert, H., Hyndman, R.D., Rogers, G.C., and Wang, K., 1994, Current deformation and the width of the seismogenic zone of the northern Cascadia subduction thrust: Journal of Geophysical Research, v. 99, p. 653–668, doi:10.1029/93JB02516.

Fleming, S.W., and Trehu, A.M., 1999, Crustal structure beneath the central Oregon convergent margin from potential-field modeling: Evidence for a buried basement ridge in local contact with a seaward dipping.:

Forsyth, D.W., Harmon, N., Scheirer, D.S., and Duncan, R.A., 2006, Distribution of recent volcanism and the morphology of seamounts and ridges in the GLIMPSE study area: Implications for the lithospheric cracking hypothesis for the origin of intraplate, non–hot spot volcanic chains: Journal of Geophysical Research: Solid Earth, v. 111, doi:https://doi.org/10.1029/2005JB004075.

Fryer, P., and Smoot, N.C., 1985, Processes of seamount subduction in the Mariana and Izu-Bonin trenches: Marine Geology, v. 64, p. 77–90, doi:10.1016/0025-3227(85)90161-6.

Gans, K.D., Wilson, D.S., and Macdonald, K.C., 2003, Pacific Plate gravity lineaments: Diffuse extension or thermal contraction? Geochemistry, Geophysics, Geosystems, v. 4, doi:https://doi.org/10.1029/2002GC000465.

GEBCO Bathymetric Compilation Group 2022, 2022, The GEBCO_2022 Grid - a continuous terrain model of the global oceans and land.: NERC EDS British Oceanographic Data Centre NOC, doi:doi:10.5285/e0f0bb80-ab44-2739-e053-6c86abc0289c.

Gerdom, M., Trehu, A.M., Flueh, E.R., and Klaeschen, D., 2000, The continental margin off Oregon from seismic investigations: Tectonophysics, v. 329, p. 79–97, doi:10.1016/S0040-1951(00)00190-6.

Goldfinger, C. et al., 2012, Turbidite event history—Methods and implications for Holocene paleoseismicity of the Cascadia subduction zone: Professional Paper, doi:10.3133/PP1661F.

Goldfinger, C., Galer, S., Beeson, J., Hamilton, T., Black, B., Romsos, C., Patton, J., Nelson, C.H., Hausmann, R., and Morey, A., 2017, The importance of site selection, sediment supply, and hydrodynamics: A case study of submarine paleoseismology on the northern Cascadia margin, Washington USA: Marine Geology, v. 384, p. 4–46, doi:10.1016/j.margeo.2016.06.008.

Goldfinger, C., Nelson, C.H., and Johnson, J.E., 2003, Holocene Earthquake Records from the Cascadia Subduction Zone and Northern San Andreas Fault Based on Precise Dating of Offshore Turbidites: Annual Review of Earth and Planetary Sciences, v. 31, p. 555–577, doi:10.1146/annurev.earth.31.100901.141246.

Govers, R., and Meijer, P.T., 2001, On the dynamics of the Juan de Fuca plate: Earth and Planetary Science Letters, v. 189, p. 115–131, doi:10.1016/S0012-821X(01)00360-0.

Hammer, P.T.C., Dorman, L.M., Hildebrand, J.A., and Cornuelle, B.D., 1994, Jasper Seamount structure: Seafloor seismic refraction tomography: Journal of Geophysical Research, v. 99, p. 6731, doi:10.1029/93JB02170.

Han, S., Carbotte, S.M., Canales, J.P., Nedimović, M.R., and Carton, H., 2018, Along-Trench Structural Variations of the Subducting Juan de Fuca Plate From

Multichannel Seismic Reflection Imaging: Journal of Geophysical Research: Solid Earth, v. 123, p. 3122–3146, doi:10.1002/2017JB015059.

Han, S., Carbotte, S.M., Canales, J.P., Nedimovic, M.R., Carton, H., Gibson, J.C., and Horning, G.W., 2016, Seismic reflection imaging of the Juan de Fuca plate from ridge to trench: New constraints on the distribution of faulting and evolution of the crust prior to subduction: Journal of Geophysical Research: Solid Earth, v. 121, p. 1849–1872, doi:10.1002/2015JB012416.

Heaton, T.H., and Hartzell, S.H., 1987, Earthquake Hazards on the Cascadia Subduction Zone: Science, v. 236, p. 162–168, doi:10.1126/SCIENCE.236.4798.162.

Heaton, T.H., and Kanamori, H., 1984, Seismic potential associated with subduction in the northwestern United States: Bulletin of the Seismological Society of America, v. 74, p. 933–941, doi:10.1785/BSSA0740030933.

Hey, R., 1977, A new class of "pseudofaults" and their bearing on plate tectonics: A propagating rift model: Earth and Planetary Science Letters, v. 37, p. 321–325, doi:10.1016/0012-821X(77)90177-7.

Horning, G., Canales, J.P., Carbotte, S.M., Han, S., Carton, H., Nedimović, M.R., and van Keken, P.E., 2016, A 2-D tomographic model of the Juan de Fuca plate from accretion at axial seamount to subduction at the Cascadia margin from an active source ocean bottom seismometer survey: Journal of Geophysical Research: Solid Earth, v. 121, p. 5859–5879, doi:10.1002/2016JB013228.

von Huene, R., and Kulm, L.D., 1973, Tectonic Summary of Leg 18, *in* Initial Reports of the Deep Sea Drilling Project, 18, U.S. Government Printing Office, doi:10.2973/dsdp.proc.18.133.1973.

Hyndman, R.D., Rogers, G.C., Dragert, H., Wang, K., Clague, J.J., Adams, J., and Bobrowsky, P.T., 1996, Giant Earthquakes Beneath Canada's West Coast: Geoscience Canada, https://journals.lib.unb.ca/index.php/GC/article/view/3896 (accessed May 2023).

Irwin, W.P., and Wallace, R.E., 1990, Geology and plate-tectonic development: The San Andreas Fault System, California, v. 1515, p. 61–80, doi:https://doi.org/10.3133/pp1515.

Kelleher, J., and McCann, W., 1976, Buoyant zones, great earthquakes, and unstable boundaries of subduction: Journal of Geophysical Research, v. 81, p. 4885–4896, doi:10.1029/JB081I026P04885.

Kellogg, J.N., Wedgeworth, B.S., Freymueller, J., Kellogg, J.N., Wedgeworth, B.S., and Freymueller, J., 1987, Isostatic compensation and conduit structures of western Pacific seamounts: Results of three-dimensional gravity modeling: GMS, v. 43, p. 85–96, doi:10.1029/GM043P0085.

Kipf, A., Hauff, F., Werner, R., Gohl, K., van den Bogaard, P., Hoernle, K., Maicher, D., and Klügel, A., 2014, Seamounts off the West Antarctic margin: A case for non-

hotspot driven intraplate volcanism: Gondwana Research, v. 25, p. 1660–1679, doi:https://doi.org/10.1016/j.gr.2013.06.013.

Kirby, S.H., Wang, K., Dunlop, Susan., Geological Survey (U.S.), Geological Survey of Canada., and University of Victoria (B.C.), 2002, The Cascadia subduction zone and related subduction systems : seismic structure, intraslab earthquakes and processes, and earthquake hazards: U.S. Dept. of the Interior, U.S. Geological Survey.

Kodaira, S., Takahashi, N., Nakanishi, A., Miura, S., and Kaneda, Y., 2000a, Subducted seamount imaged in the rupture zone of the 1946 Nankaido earthquake: Science, v. 289, p. 104–106, doi:10.1126/SCIENCE.289.5476.104.

Kodaira, S., Takahashi, N., Nakanishi, A., Miura, S., and Kaneda, Y., 2000b, Subducted Seamount Imaged in the Rupture Zone of the 1946 Nankaido Earthquake: Science, v. 289, p. 104–106, doi:10.1126/SCIENCE.289.5476.104.

Kreemer, C., Blewitt, G., and Klein, E.C., 2014, A geodetic plate motion and Global Strain Rate Model: Geochemistry, Geophysics, Geosystems, v. 15, p. 3849–3889, doi:10.1002/2014GC005407.

Kulm, L.D. et al., 1973, Site 174, *in* Initial Reports of the Deep Sea Drilling Project, 18, U.S. Government Printing Office, doi:10.2973/dsdp.proc.18.105.1973.

Lee, M., Carbotte, S.M., Shuck, B., Han, S., Boston, B., Lee, M., Carbotte, S.M., Shuck, B., Han, S., and Boston, B., 2022, Examining sediment consolidation state and hydrothermal circulation at and near buried seamounts on the Cascadia Margin and

its relation to earthquake generation: AGUFM, v. 2022, p. T42D-0147, https://ui.adsabs.harvard.edu/abs/2022AGUFM.T42D0147L/abstract (accessed May 2023).

Lillie, R.J., 1998, Whole Earth Geophysics: An Introductory Textbook for Geologists and Geophysicists:

Ludwin, R.S., Dennis, R., Carver, D., McMillan, A.D., Losey, R., Clague, J., Jonientz-Trisler, C., Bowechop, J., Wray, J., and James, K., 2005, Dating the 1700 Cascadia Earthquake: Great Coastal Earthquakes in Native Stories: Seismological Research Letters, v. 76, p. 140–148, doi:10.1785/GSSRL.76.2.140.

Mazzotti, S., 2004, Variability of Near-Term Probability for the Next Great Earthquake on the Cascadia Subduction Zone: Bulletin of the Seismological Society of America, v. 94, p. 1954–1959, doi:10.1785/012004032.

McCaffrey, R., Qamar, A.I., King, R.W., Wells, R., Khazaradze, G., Williams, C.A., Stevens, C.W., Vollick, J.J., and Zwick, P.C., 2007, Fault locking, block rotation and crustal deformation in the Pacific Northwest: Geophysical Journal International, v. 169, p. 1315–1340, doi:10.1111/j.1365-246X.2007.03371.x.

McCrory, P.A., 2000, Upper plate contraction north of the migrating Mendocino triple junction, northern California: Implications for partitioning of strain: Tectonics, v. 19, p. 1144–1160, doi:10.1029/1999TC001177.

Melgar, D., 2021, Was the January 26th, 1700 Cascadia Earthquake Part of a Rupture Sequence? Journal of Geophysical Research: Solid Earth, v. 126, p. e2021JB021822, doi:10.1029/2021JB021822.

Menichelli, I., Corbi, F., Brizzi, S., Rijsingen, E. van, Lallemand, S., and Funiciello, F., 2023, Seamount Subduction and Megathrust Seismicity: The Interplay Between Geometry and Friction: Geophysical Research Letters, v. 50, p. e2022GL102191, doi:10.1029/2022GL102191.

Miller, M.M., Melbourne, T., Johnson, D.J., and Sumner, W.Q., 2002, Periodic slow earthquakes from the Cascadia subduction zone: Science, v. 295, p. 2423, doi:10.1126/SCIENCE.1071193.

Mochizuki, K., Yamada, T., Shinohara, M., Yamanaka, Y., and Kanazawa, T., 2008, Weak interplate coupling by seamounts and repeating M ∼ 7 earthquakes: Science, v. 321, p. 1194–1197, doi:10.1126/SCIENCE.1160250.

Nedimović, M.R., Bohnenstiehl, D.W.R., Carbotte, S.M., Pablo Canales, J., and Dziak, R.P., 2009, Faulting and hydration of the Juan de Fuca plate system: Earth and Planetary Science Letters, v. 284, p. 94–102, doi:10.1016/j.epsl.2009.04.013.

Nelson, A.R. et al., 1995, Radiocarbon evidence for extensive plate-boundary rupture about 300 years ago at the Cascadia subduction zone: Nature, v. 378, p. 371–374, doi:10.1038/378371a0.

Northwest Geophysical Associates Inc., 2004, User's Guide GM-SYS ® User's Guide Revision 4:, www.nga.com.

Parsons, T. et al., 2005, Crustal Structure of the Cascadia Fore Arc of Washington:, http://pubs.usgs.gov/pp/pp1661-D.

Perfettini, H. et al., 2010, Seismic and aseismic slip on the Central Peru megathrust: Nature 2010 465:7294, v. 465, p. 78–81, doi:10.1038/nature09062.

Perfettini, H., and Ampuero, J.P., 2008, Dynamics of a velocity strengthening fault region: Implications for slow earthquakes and postseismic slip: Journal of Geophysical Research: Solid Earth, v. 113, p. 9411, doi:10.1029/2007JB005398.

Porritt, R.W., Allen, R.M., Boyarko, D.C., and Brudzinski, M.R., 2011, Investigation of Cascadia segmentation with ambient noise tomography: Earth and Planetary Science Letters, v. 309, p. 67–76, doi:10.1016/J.EPSL.2011.06.026.

Prytulak, J., Vervoort, J.D., Plank, T., and Yu, C., 2006, Astoria Fan sediments, DSDP site 174, Cascadia Basin: Hf–Nd–Pb constraints on provenance and outburst flooding: Chemical Geology, v. 233, p. 276–292, doi:10.1016/J.CHEMGEO.2006.03.009.

Rasmissen, R., and Pedersen, L.B., 1979, End corrections in potential field modeling: Geophysical Prospecting, v. 27, p. 749–760, doi:10.1111/j.1365-2478.1979.tb00994.x.

Robinson, D.P., Das, S., and Watts, A.B., 2006, Earthquake rupture stalled by a subducting fracture zone: Science, v. 312, p. 1203–1205, doi:10.1126/SCIENCE.1125771.

Rogers, G.C., 1988, An assessment of the megathrust earthquake potential of the Cascadia subduction zone 1:, doi:https://doi.org/10.1139/e88-083.

Rogers, A.M., Walsh, T.J., Kockelman, W.J., Priest, G., Weaver, C.S., and Shedlock2, K.M., 1991, Estimates of seismic source regions from considerations of the earthquake distribution and regional tectonics in the Pacific Northwest: Open-File Report, doi:10.3133/OFR91441R.

Ryan, W.B.F. et al., 2009, Global multi-resolution topography synthesis: Geochemistry, Geophysics, Geosystems, v. 10, doi:10.1029/2008GC002332.

Sandwell, D.T., and Dunbar, J.A., 1988, Stretching of the central Pacific lithosphere: Super swell, crossgrain lineations and en-echelon ridges: Eos Trans. AGU, v. 69, p. 1429.

Sandwell, D., and Fialko, Y., 2004, Warping and cracking of the Pacific plate by thermal contraction: Journal of Geophysical Research: Solid Earth, v. 109, doi:https://doi.org/10.1029/2004JB003091.

Sandwell, D.T., Müller, R.D., Smith, W.H.F., Garcia, E., and Francis, R., 2014, New global marine gravity model from CryoSat-2 and Jason-1 reveals buried tectonic structure: Science, v. 346, p. 65–67, doi:10.1126/SCIENCE.1258213.

Sandwell, D.T., Winterer, E.L., Mammerickx, J., Duncan, R.A., Lynch, M.A., Levitt, D.A., and Johnson, C.L., 1995, Evidence for diffuse extension of the Pacific Plate from Pukapuka ridges and cross-grain gravity lineations: Journal of Geophysical Research: Solid Earth, v. 100, p. 15087–15099, doi:https://doi.org/10.1029/95JB00156.

Satake, K., 2003, Fault slip and seismic moment of the 1700 Cascadia earthquake inferred from Japanese tsunami descriptions: Journal of Geophysical Research, v. 108, p. 2535, doi:10.1029/2003JB002521.

Satake, K., Shimazaki, K., Tsuji, Y., and Ueda, K., 1996, Time and size of a giant earthquake in Cascadia inferred from Japanese tsunami records of January 1700: Nature 1996 379:6562, v. 379, p. 246–249, doi:10.1038/379246a0.

Schmalzle, G.M., McCaffrey, R., and Creager, K.C., 2014, Central Cascadia subduction zone creep: Geochemistry, Geophysics, Geosystems, v. 15, p. 1515–1532, doi:10.1002/2013GC005172.

Schmidt, R., Schmincke, H.-U., and Sigurdsson, H., 2000, Seamounts and island building: Encyclopedia of volcanoes, p. 383–402.

Scholz, C., Geology, C.S.-, and 1997, undefined, 1997, The effect of seamount subduction on seismic coupling: pubs.geoscienceworld.org, p. 487, https://pubs.geoscienceworld.org/gsa/geology/article-abstract/25/6/487/206650?casa_token=YQlFu-

Hel_sAAAAA:LUojEv5767905i6wW-iFhyVajsz7mzRuDtPC_EpJHVLZbXugkvs4TMez_iYbbaJME02rhIM (accessed May 2023).

Scholz, C.H., and Small, C., 1997, The effect of seamount subduction on seismic coupling:, http://pubs.geoscienceworld.org/gsa/geology/article-pdf/25/6/487/3516907/i0091-7613-25-6-487.pdf.

Shih, J., and Molnar, P., 1975, Analysis and implications of the sequence of ridge jumps that eliminated the Surveyor Transform Fault: Journal of Geophysical Research, v. 80, p. 4815–4822, doi:10.1029/JB080I035P04815.

Singh, S.C. et al., 2011, Aseismic zone and earthquake segmentation associated with a deep subducted seamount inSumatra: Nature Geoscience, v. 4, p. 308–311, doi:10.1038/ngeo1119.

Song, T.R.A., and Simons, M., 2003, Large trench-parallel gravity variations predict seismogenic behavior in subduction zones: Science, v. 301, p. 630–633, doi:10.1126/SCIENCE.1085557/SUPPL_FILE/SONGSOM.PDF.

Stern, R.J., 2002, Subduction Zones: Reviews of Geophysics, v. 40, p. 3–1, doi:10.1029/2001RG000108.

Talwani, M., and Heirtzler, J.R., 1964, Computation of magnetic anomalies caused by two dimensional structures of arbitary shape: Computers in the mineral industries, v. 1, p. 464–480.

Talwani, M., Worzel, J.L., and Landisman, M., 1959, Rapid gravity computations for two-dimensional bodies with application to the Mendocino submarine fracture zone: Journal of Geophysical Research, v. 64, p. 49–59, doi:10.1029/JZ064i001p00049.

Telford, W.M., Geldart, L.P., and Sheriff, R.E., 1990, Applied Geophysics: Applied Geophysics, doi:10.1017/CBO9781139167932.

Tominaga, M., 2017a, Gravimeter (Bell BGM-3) data as collected during the cruise RR1718, Collaborative EAGER project: Early Career Seismic Chief Scientist Training Cruise. Rolling Deck to Repository (R2R):, doi:10.7284/128301.

Tominaga, M., 2017b, Magnetometer (MarineMagnetics SeaSPY) data as collected during the cruise RR1718, Collaborative EAGER project: Early Career Seismic Chief Scientist Training Cruise. Rolling Deck to Repository (R2R):, doi:10.7284/128302.

Tominaga, M., Trehu, A., and Lyle, M., 2018, Multi-Channel Seismic Shot Data from the Seismic Early Career Chief Scientist Training Cruise 2017, Cascadia Margin, acquired during R/V Roger Revelle expedition RR1718 (2017). IEDA:, doi:10.1594/IEDA/324504.

Tozer, B., Sandwell, D.T., Smith, W.H.F., Olson, C., Beale, J.R., and Wessel, P., 2019, Global Bathymetry and Topography at 15 Arc Sec: SRTM15+: Earth and Space Science, v. 6, p. 1847–1864, doi:10.1029/2019EA000658.

Trehu, A.M., Asudeh, I., Brocher, T.M., Luetgert, J.H., Mooney, W.D., Nabelek, J.L., and Nakamura, Y., 1994, Crustal Architecture of the Cascadia Forearc: Science, v. 266, p. 237–243, doi:10.1126/SCIENCE.266.5183.237.

Trehu, A.M., Blakely, R.J., and Williams, M.C., 2012, Subducted seamounts and recent earthquakes beneath the central cascadia forearc: Geology, v. 40, p. 103–106, doi:10.1130/G32460.1.

Trehu, A.M., Bohrmann, G., Torres, M.E., and Colwell, F.S., 2006, Proceedings of the Ocean Drilling Program, 204 Scientific Results: Ocean Drilling Program, v. 199, doi:10.2973/odp.proc.sr.204.2006.

Trehu, A.M., Braunmiller, J., and Davis, E., 2015, Seismicity of the Central Cascadia Continental Margin near 44.5 N: A Decadal View: Seismological Research Letters, v. 86, p. 819–829, doi:10.1785/0220140207.

Wang, K., and Bilek, S.L., 2011, Do subducting seamounts generate or stop large earthquakes? Geology, v. 39, p. 819–822, doi:10.1130/G31856.1.

Wang, K., and Bilek, S.L., 2014, Invited review paper: Fault creep caused by subduction of rough seafloor relief: Tectonophysics, v. 610, p. 1–24, doi:10.1016/J.TECTO.2013.11.024.

Watts, A.B., Grevemeyer, I., Shillington, D.J., Dunn, R.A., Boston, B., and Gómez de la Peña, L., 2021, Seismic Structure, Gravity Anomalies and Flexure Along the

Emperor Seamount Chain: Journal of Geophysical Research: Solid Earth, v. 126, p. e2020JB021109, doi:10.1029/2020JB021109.

Watts, A.B., and Ribe, N.M., 1984, On geoid heights and flexure of the lithosphere at seamounts: Journal of Geophysical Research: Solid Earth, v. 89, p. 11152–11170, doi:10.1029/JB089IB13P11152.

Weaver, C.S., and Shedlock, K.M., 1991, Estimates of seismic source regions from considerations of the earthquake distribution and regional tectonics in the Pacific Northwest:, doi:10.3133/ofr91441R.

Weigel, W., and Grevemeyer, I., 1999, The Great Meteor seamount: seismic structure of a submerged intraplate volcano: Journal of Geodynamics, v. 28, p. 27–40, doi:10.1016/S0264-3707(98)00030-1.

West, M., Menke, W., and Tolstoy, M., 2003, Focused magma supply at the intersection of the Cobb hotspot and the Juan de Fuca ridge: Geophysical Research Letters, v. 30, doi:10.1029/2003GL017104.

Westbrook, G.K., Carson, B., and Musgrave, R.J., 1994, Proceedings of the Ocean Drilling Program, 146 Part 1 Initial Reports (G. K. Westbrook, B. Carson, & R. J. Musgrave, Eds.): Ocean Drilling Program, v. 146–1, doi:10.2973/odp.proc.ir.146-1.1994.

Wilcock, W.S.D., Tolstoy, M., Waldhauser, F., Garcia, C., Tan, Y.J., Bohnenstiehl, D.R., Caplan-Auerbach, J., Dziak, R.P., Arnulf, A.F., and Mann, M.E., 2016, Seismic

constraints on caldera dynamics from the 2015 Axial Seamount eruption: Science, v. 354, p. 1395–1399, doi:10.1126/science.aah5563.

Wilson, D.S., 1988, Tectonic history of the Juan de Fuca Ridge over the last 40 million years: Journal of Geophysical Research, v. 93, doi:10.1029/jb093ib10p11863.

Wilson, D.S., 2002, The Juan de Fuca plate and slab: isochron structure and Cenozoic plate motions:, doi:10.4095/222387.

Won, I.J., and Bevis, M., 1987, Computing the gravitational and magnetic anomalies due to a polygon: Algorithms and Fortran subroutines: GEOPHYSICS, v. 52, p. 232–238, doi:10.1190/1.1442298.

Appendix

A) Reprocessing MCS data from raw data:

The following steps were performed in SeismicUNIX:
(The original script was provided for the 2017 Seismic ECS Cruise by G. Mountain, edits by K. Davenport and B. Phrampus)

1. Convert the SEGY files to SU format.
2. Separate the non-zero header values from the data file and store them in a text file.
3. Remove the auxiliary channels 49-52 (Channel 49 detects pressure waves from acoustic sources, while channels 50 through 52 are open channels).
4. Remove 50 ms time shift between trigger and airgun.
5. An additional 0.1 ms of data from the end of recording time was edited out in this step. It was performed to further reduce the amount of artifacts in the data.
6. Bandpass filter using corner frequencies 15-25-350-500 to remove low and high frequency noise.
7. Trace editing: Write trace offsets to headers.
8. Geometry assignment: Write CDP numbers to headers.
9. CDP sorting and checking that CDP numbers are assigned properly.
10. Velocity analysis.
11. Normal Moveout (NMO) correction: Due to erroneous results from velocity analysis, I used constant velocity of 1500 m/s for NMO correction.
12. Stacking
13. Migration: Stolt migration method was used with constant water velocity of 1500 m/s.

The bash script for this whole process using SeismicUNIX is as follows:

```
#!/bin/bash

# Automated processing using basic parameters
# 28 Sept 2017
# B Phrampus, K Davenport
#=========================================================
# Steps:
#  1. Read in segy
#  2. Remove auxiliary channels 49-52
#  3. Kill bad channels (bird noise on 1,17,33)
#  4. Remove 50 ms pre-bubble time
#  5. Write geometry
#  6. Write CMP numbers
#  7. Bandpass filter
#  8. Sort by CMPs
#  9. Spherical Divergence correction
# 10. NMO correction
# 11. Stack
# 12. Migration (via sioseis and SU)
# 13. Layback correction
# 14. Write sorted, stacked, and migrated files in .su and. sgy

### Get input parameters from the command line
#=========================================================
echo -n "Line number? (Name format: site_RR1718_line_[number].sgy)  "
read i
echo "Line $i"

echo -n "Default zero phase bandpass filter? (y/n)  "
read filt
if [[ $filt == y ]]; then
      fl1=15; fl2=25; fh1=250; fh2=500
      butter="n"
      echo "Using zero phase bandpass 15-25-250-500"
elif [[ $filt == n ]]; then
      echo -n "Minimum phase Butterworth filter? (y/n)  "
      read butter
      echo "Enter bandpass corner frequencies:  "
      read fl1 fl2 fh1 fh2
      if [[ $butter == n ]]; then
            echo -n "Using zero phase bandpass filter ${fl1}-${fl2}-
${fh1}-${fh2}"
      elif [[ $butter == y ]]; then
            echo -n "Using minimum phase Butterworth filter ${fl1}-
${fl2}-${fh1}-${fh2}"
      fi
fi

### Prepare SU file from SEG-Y
#=========================================================
```

```
file="RR1718_line_$i"

echo "~~~ Begin processing site_${file}.sgy"

segyread tape=site_${file}.sgy | \
segyclean | \
suwind key=tracf min=1 max=48 | \
sukill key=tracf a=1 | sukill key=tracf a=17 | sukill key=tracf a=33 |
\
sushw key=delrt a=-50 | \
sushift tmin=0.0 tmax=7.95 | \
sushw key=offset a=80.25 b=12.5 j=48  > tmp1.su

# set recording delay (delrt) to -50 ms
# time shift to remove first 50 ms, now starttime=0.0 endtime=7.95

# Find min and max shot numbers

shot1=`surange < tmp1.su key=ep | tail -n1 | awk '{print $2}'`
shot2=`surange < tmp1.su key=ep | tail -n1 | awk '{print $3}'`
num_chan=`surange < tmp1.su key=tracf | tail -n1 | awk '{print $3}'`
atmp=$((${num_chan} + 1001 - ${shot1} * 4))

echo "~~~ File prep complete. Begin filtering"

### Begin processing sequence
#============================================================
# Filter paramters are read from command line
if [[ $butter == n ]]; then
      sufilter < tmp1.su f=$fl1,$fl2,$fh1,$fh2 > tmp2.su
      name="bp${fl1}-${fl2}-${fh1}-${fh2}"
elif [[ $butter == y ]]; then
      subfilt < tmp1.su zerophase=1 fstoplo=$fl1 fpasslo=$fl2
fpasshi=$fh1 \
            fstophi=$fh2 > tmp2.su
      name="bwth${fl1}-${fl2}-${fh1}-${fh2}"
fi

### Sort on CMPs and apply spherical divergence correction
#============================================================
echo "~~~ Headers complete. Begin sorting and spherical divergence
correction"
suchw < tmp2.su key1=cdp key2=ep key3=tracf a=$atmp b=4 c=-1 > tmp3.su
susort < tmp3.su cdp offset | sudivcor > ${file}_${name}_sort.su

### Find max cdp number
cdp2=`surange < tmp3.su key=cdp | tail -n1 | awk '{print $3}'`

### Apply NMO correction and stack
#============================================================
```

```
echo "~~~ Sorting complete. Begin NMO correction and stack"
sunmo < ${file}_${name}_sort.su vnmo=1500 | \
sustack > ${file}_${name}_stack.su

# apply layback and write to headers.(***must need the Generic Mapping
Tools installed)
#=============================================================
echo "~~~ Applying lackback correction"
./layback_correction.sh $file $name

# Clean up and Organize
mv ${file}_${name}_sort_lb.su ${file}_${name}_sort.su
mv ${file}_${name}_stack_lb.su ${file}_${name}_stack.su

#=============================================================
### Migration
#=============================================================

### MIGRATE (WATER VELOCITY) USING SIOSEIS
#=============================================================
# **** Comment out this section if you do not have sioseis installed
****
# write out segy of stack lines for sioseis migration
#segyhdrs < ${file}_${name}_stack.su
#segywrite < ${file}_${name}_stack.su tape=${file}_${name}_stack.sgy
#echo "~~~ Stacking complete. Beginning SIOSEIS migration script
fkmig.sioin"
#./fkmig.sioin ${file}_${name}
#echo "~~~ Sioseis migration complete"
# read in new migrated segyfile
#segyread tape=${file}_${name}_fkmig1500.sgy | segyclean >
${file}_${name}_fkmig1500.su

### SU Stolt Migration
#=============================================================
# Apply anti-alias filter, resample, and migrate for comparison.
# Original data dt=0.0005 nt=16000; resample to dt=0.002

sufilter < ${file}_${name}_stack.su f=100,200 amps=1,0 | \
suresamp rf=0.25 | \
sustolt cdpmin=1 cdpmax=$cdp2 dxcdp=6.25 tmig=0.0 \
    vmig=1500 smig=1.0 > ${file}_${name}_stolt_resamp.su

echo "~~~ Migration complete. Plotting results"

# plot migrated sections
#suximage < ${file}_${name}_fkmig1500.su perc=99 title="SIOSEIS" &
suximage < ${file}_${name}_stolt_resamp.su perc=99 title="SUSTOLT" &
#=============================================================
# Text files for QC
surange < ${file}_${name}_sort.su > ${file}_${name}_range.txt
sukeycount < ${file}_${name}_sort.su key=cdp > ${file}_${name}_fold.txt
```

```
suwind < ${file}_${name}_stack.su  key=tracf min=1 max=1 | sugethw
output=geom \
      key=year,day,hour,minute,sec,ep,sx,sy >
${file}_${name}_location.txt

#=========================================================
echo "~~~ Writing and organizing files"

# Write sorted segy file
segyhdrs < ${file}_${name}_sort.su
segywrite < ${file}_${name}_sort.su tape=${file}_${name}_sort.sgy

# write out stack lines
segyhdrs < ${file}_${name}_stack.su
segywrite < ${file}_${name}_stack.su tape=${file}_${name}_stack.sgy

# write out fkmig1500 lines
#segyhdrs < ${file}_${name}_fkmig1500.su
#segywrite < ${file}_${name}_fkmig1500.su
tape=${file}_${name}_fkmig1500.sgy

# write out stolt migrated lines
segyhdrs < ${file}_${name}_stolt_resamp.su
segywrite < ${file}_${name}_stolt_resamp.su
tape=${file}_${name}_stolt_resamp.sgy

rm temphdr tmp1.su tmp2.su tmp3.su binary header gmt.conf gmt.history \
      RR1718_line_*tmp*.txt RR1718_line_*tmp.bin

[ ! -e Final_Processed/ ] && mkdir Final_Processed/
[ ! -e Final_Processed/Info ] && mkdir Final_Processed/Info/
[ ! -e Final_Processed/Info/maps ] && mkdir Final_Processed/Info/maps

for f in sgy su; do
      [ ! -e Final_Processed/$f/ ] && mkdir Final_Processed/$f
      for j in sort stack fkmig1500 stolt_resamp; do
            [ ! -e Final_Processed/$f/$j/ ] && mkdir
Final_Processed/$f/$j
            mv ${file}_${name}_${j}.${f} Final_Processed/$f/$j/.
      done
done

mv ${file}_${name}_*.txt Final_Processed/Info/.
mv ${file}_${name}_*.ps Final_Processed/Info/maps/.

#=========================================================
echo "~~~ Organizing files complete. End script"
echo "~~~~~~~~~~~~~~~~~~~~~~~~~~~~~~~~~~~~~~~~~~~~~~~~~"
```